https://doi.org/10.5194/egusphere-2025-4698
Preprint. Discussion started: 26 September 2025

Structural joint modeling of magnetotelluric data and Rayleigh wave dispersion curves using Pareto-based particle swarm optimization: An example to delineate the crustal structure of the southeastern part of the Biga Peninsula in western Anatolia

Ersin Büyük[1,2], Ekrem Zor[2], Mustafa Cengiz Tapırdamaz[2]

[1]Department of Geophysical Engineering, Gümüşhane University, Gümüşhane, 29100, Türkiye
[2]TÜBİTAK Marmara Research Center, Earth Sciences Research Group, Kocaeli, 41470, Türkiye

Correspondence to: Ersin Büyük (ebuyuk@gumushane.edu.tr)

Abstract. It is well known that the joint inversion of magnetotelluric and seismological data sets improves the solution quality of the crustal structure, even if the electrical resistivity and seismic velocity parameters are not physically well correlated. The structurally coupled joint inversion approach has received much attention in the last two decades to estimate such parameters with penalizing their cross-gradient vectors at similar spatial positions. Despite this interest, various structural couplings and different physical directions (incremental or decremental) have been partially overlooked. We propose an approach for the joint inversion of magnetotelluric (MT) and Rayleigh wave dispersion (RWD) data to estimate uncorrelated parameters by integrating particle swarm optimization (PSO) and the Pareto optimality approach. We used these methods optimality to overcome difficulties encountered in traditional joint inversion algorithms and to obtain optimum solutions having same and/or different physical directions. The good correlation between the inverted and synthetic models produced noise-free and noisy data further strengthened our confidence in the modelling of the field data from the southeastern Biga Peninsula in western Anatolia. The models inverted from the field data, which are in consistent with previous studies, confirm the usefulness of the presented method. A remarkable feature of the presented method is the estimation of uncorrelated physical parameters such as electrical resistivity and seismic velocity without penalizing. Therefore, the presented method not only offers advantages in joint inversion but also allows modelers to observe and analyze model parameters having different sensitivities that may indicate different physical directions.

1 Introduction

Joint inversion studies are becoming increasingly popular to reduce the non-uniqueness by constraining the solution, to improve the solution quality, and to determine models having structures that are difficult to solve. A growing body of literature investigated the joint inversion of different geophysical data sensitive to different physical phenomena to improve subsurface images so far (e.g., Dell'Aversana et al. 2016; Gallardo 2004; Lelièvre et al. 2012; Meju and Gallardo 2016; Stefano et al. 2011). The joint inversion of MT and RWD data has also been attempted by researchers to estimate more accurate physical parameters, to provide valuable information in modelling of the crustal structure (Aquino et al. 2022;

https://doi.org/10.5194/egusphere-2025-4698
Preprint. Discussion started: 26 September 2025

Manassero et al. 2020; Moorkamp, Jones, and Fishwick 2010; Roux et al. 2011; Wu et al. 2018, 2020, 2022), to show their complementary relationships for the solution (Afonso et al., 2013), and to provide a direct link to geology by imaging the rock properties (Takougang et al., 2015). Furthermore, in recent studies such as Ogaya et al. (2016); Wu et al. (2018); Hu et al. (2024) demonstrated that joint inversion of such datasets is advantageous over single inversion methods, as it improves the accuracy, resolution and interpretability of subsurface models. These studies show that the joint inversion of MT and RWD data significantly improved inversion results, even if inconsistencies existed between electrical and seismic boundaries in the spatial domain. This highlights how integration of multiple seismological and magnetotelluric datasets can provide a more coherent picture of the subsurface, as each method contributes unique information that can help to resolve uncertainties that exist in single-method inversions.

In the joint inversion of such datasets, electrical resistivity and seismic velocity parameters, which are not physically well correlated (Carcione et al., 2007), are generally estimated in two ways: 1) structurally coupled, and 2) petrophysical joint inversion. Structurally coupled joint inversion approaches are based on the assumption that the directions of changing physical parameters are penalized by a structural term (Gallardo and Meju 2003; Moorkamp et al. 2013). As an effective method, Gallardo and Meju (2003) and Gallardo (2004) applied a cross-gradient approach, which aims to penalize model gradient vectors in different directions. This method promotes the models that exhibit spatial changes at similar spatial positions. However, since one cannot be sure that seismic velocity and electrical resistivity parameters respond to the same or similar degree at similar spatial locations, different structural couplings may need to be considered as indicated by Wagner and Uhlemann (2021). For example, small fractions of conductive material can significantly affect bulk resistivity, while seismic velocities are strongly affected by large volumes of rocks (Moorkamp et al., 2010; Simpson and Bahr, 2005). Therefore, such incompatible models should also be considered, according to which the seismic velocity pattern remains almost unchanged despite the conductive layers. On the other hand, the cross-gradient approach also requires model gradient vectors, it may not be useful in the one-dimensional case where the resistivity and velocity parameters only change in the *z*-direction that exhibit zero cross-gradients (Li et al. 2019; Wu et al. 2018). The petrophysical joint inversion is based on the direct estimation of petrophysical parameters from geophysical parameters obtained from inversion algorithms (Mollaret et al., 2020; Steiner et al., 2021). The major problem with linking the geophysical parameters to petrophysical relationship is that their physical meaning cannot be guaranteed (Wagner and Uhlemann, 2021). This is because seismic velocities and electrical resistivities may respond differently to petrophysical properties such as porosity, permeability and temperature in the crustal zone (Afonso et al., 2013; Chen et al., 2012; Gao et al., 2012). The nonlinear and unpredictable relationship between these parameters prevents a full correlation as they are strongly influenced by the rock properties in a specific study area (Linde and Sacks, 1998; Mavko et al., 1998). Therefore, it is generally a challenge to achieve a mutual coupling between such physical parameters with different sensitivities (Aquino et al., 2022).

Joint inversion techniques used in both structural and petrophysical approaches also require simultaneously minimization of objective functions given by the misfits of different data sets. These techniques generally based on a derivative-based

https://doi.org/10.5194/egusphere-2025-4698
Preprint. Discussion started: 26 September 2025

approach, which leads to a dependence on an initial model and local minima entrapment (Moorkamp et al., 2007) for both MT (Constable et al., 1987; Smith and Booker, 1988) and RWD (Dorman and Ewing, 1962) modeling. However, Particle Swarm Optimization (PSO), one of the modern global optimization methods, is increasingly becoming a useful method for modeling geophysical data to overcome these disadvantages. A striking feature of the PSO, as well as other global optimization methods such as the Genetic Algorithm (GA) (Goldberg and Holland, 1988), Neighbourhood Algorithm (NA) (Sambridge, 1999) and Simulated Annealing (SA) (Kirkpatrick et al., 1983), is the elimination of the trapping of local minima and/or initial model dependence that generally occurs in traditional inversion techniques (Pace et al., 2021). In these global optimization methods, it is necessary to use improved constraints to broadly explore the space of possible models and verify that the set of acceptable models has been reduced (Gupta et al., 2023b). However, additional geophysical datasets can effectively reduce the set of acceptable models for such a global optimization that searches too large a model space, and thus increase the reliability of subsurface interpretations (Moorkamp et al., 2010). This allows a further advantage in reducing the model space, which provides meaningful models when global optimization algorithms are used. However, one of the other drawbacks of the joint inversion techniques used is the combination of objective functions that requires appropriate weights (Bijani et al., 2017). In this case, subjective and unpredictable weightings of the objective functions can lead to a misleading result (Büyük et al., 2020; Kozlovskaya et al., 2007; Lines et al., 1988). As an effective method, Moore (1897) identified a definition of Pareto optimality approach presenting Pareto-optimum solution set to summarize all solutions given by each objective function without combining with different weights (Baumgartner et al., 2004).

In this paper, an approach for the joint inversion of MT and RWD data is proposed that takes advantage of the integration of multiobjective PSO with the Pareto optimality approach (hereafter referred to as Pareto-MOPSO). Apart from Moorkamp et al. (2010); Roux et al. (2011) and Wu et al. (2022), who used GA in combination with Pareto optimality, we utilized PSO with a fast convergence rate compared to GA (Büyük et al. 2017; Gill et al. 2006; James Kennedy and Spears 1998; Yuan et al. 2009). In structurally coupled joint inversion, the physical parameters in the model space are estimated with or without prescribing the spatial locations on the common layer, grid or volume depending on the dimensional analysis (Haber and Oldenburg, 1997; Wagner and Uhlemann, 2021). In this study, common layer thicknesses of the one-dimensional models estimated by PSO provided a structurally constraint on the seismic velocity and electrical resistivity parameters, as described by Wu et al. (2018). However, no coupling or penalizing was applied to physical parameters that are also estimated by PSO in the common layers. In this way, we aimed to obtain solutions with same and/or different physical directions from the distribution of the Pareto-optimal solution set. On the other hand, we used a many-layered resistivity-depth and velocity-depth functions, unlike to Wu et al. (2018), who present modeling with few layers that may suppress important structures (Vozoff, 1990; Weaver and Agarwal, 1993).

As a first step, some synthetic analyses with noise-free and noisy data were performed with compatible and incompatible resistivity and seismic velocity models to confirm the applicability of the approach. We obtained many models by the means of the Pareto-optimal solution set. However, a notable feature of the statistical distributions of the solution set was that the mean values of the estimated physical parameters were closer to the synthetic model and had the same physical direction as the synthetic model. These tests highlighted that the inverted models reproduced the synthetic models in a good agreement. In the second step, RWD data obtained from paths between specific pairs of seismic stations and MT data over the paths in the southeastern part of the Biga Peninsula in Anatolia were jointly modelled by following the approaches used in the synthetic analysis. The results from field data in conjunction with previous field studies confirmed that the presented approach can be used for joint inversion of datasets having different sensitivities. Therefore, different physical directions can be observed and obtained without penalizing Sof the parameters, which are estimated by PSO. Moreover, reliable results can be obtained by Pareto-MOPSO regardless of the above-mentioned drawbacks that are the traditional derivative-based algorithms and the combination of objective function terms.

2 Optimization Methods

2.1 Particle Swarm Optimization

PSO is a modern global optimization method introduced by Kennedy and Eberhart (1995) and is inspired by the movements of flocks of birds or fish to reach the goal by the shortest route. In the PSO method, the particles, denoted by a vector of model parameters in the m-dimensional model space $\boldsymbol{x} = [x_1, x_2, x_3, \dots \dots \dots x_m]$ within a feasible search area (Figure 1a), take a position in the one-dimensional objective space $\Phi(\boldsymbol{x})$ as illustrated in Figure 1b. As an example, of a minimization problem, the particles that communicate and learn with each other change their positions with a velocity vector in the model space as follows:

$$\boldsymbol{V}_i^{k+1} = \omega \boldsymbol{V}_i^k + c_1\gamma_1 \otimes \left(\boldsymbol{x}_{pbest,i} - \boldsymbol{x}_i^k\right) + c_2\gamma_2 \otimes \left(\boldsymbol{x}_{gbest} - \boldsymbol{x}_i^k\right). \tag{1}$$

therefore, new position can be obtained in the following way:

$$\boldsymbol{x}_i^{k+1} = \boldsymbol{x}_i^k + \boldsymbol{V}_i^{k+1}, \tag{2}$$

where, subscript i is the number of particles and k is the number of iterations. The position and velocity vector of a particle i at iteration k are represented as $\boldsymbol{x}_i^k$ and $\boldsymbol{V}_i^k$, respectively. ω is the inertia weight term forced on the velocity vector. c_1 and c_2 are the acceleration factors of the local and global learning constants, γ_1 and γ_2 are uniformly random numbers in the range [0,1]. The particle that has the best fit of all evaluated particles is set as the global leader. If a particle position changed with a new velocity vector is a more optimal solution than the previous best solution determined by an objective function, the particle replaces its previous position with the new one assigned as $\boldsymbol{x}_{pbest}$. If a particle represents a more optimal solution than the global best solution, the particle is assigned as $\boldsymbol{x}_{gbest}$ (Büyük and Karaman, 2024). These processes are reiterated until the maximum number of iterations or the minimum error criterion specified by the user is satisfied (Engelbrecht, 2007).

Towards the end of the optimization process, all particles close to the global minimum in the objective space as illustrated in Figure 1c.

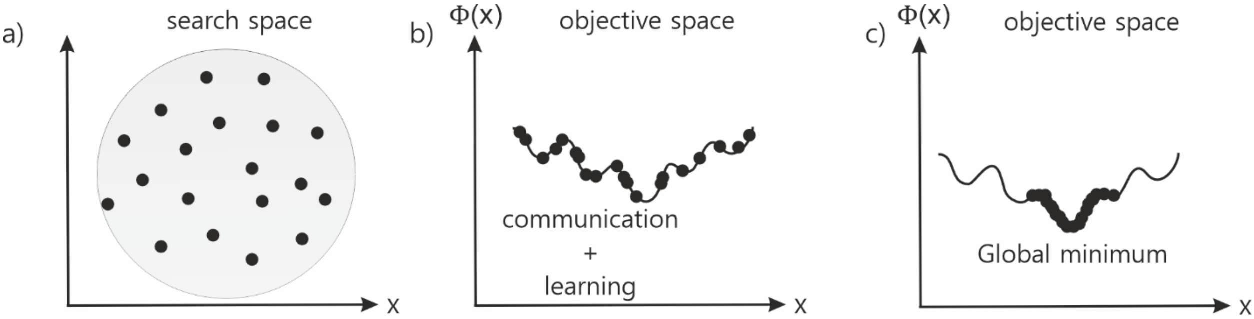

Figure 1: Schematic illustration of randomly distributed particles in model space within a feasible parameter search space (a), projection of the particles onto the objective function space (b), convergence of the particles to the global minimum (c), modified from Büyük (2021)**.**

To overcome drawbacks of traditional methods of inversion, PSO has seen a tremendous upsurge in the last decade to invert geophysical data, such as DC-resistivity data (e.g., Juan L. Fernández Martínez et al. 2010; Peksen et al. 2014; Shaw and Srivastava 2007), self-potential data (e.g., Fern and Garc 2010; Monteiro Santos 2010; Peksen et al. 2011), gravity data (e.g., Essa et al. 2021; Pallero et al. 2015), time-domain electromagnetic data (e.g., Amato et al. 2021; Pace et al. 2022), magnetotelluric data (e.g., Grandis and Maulana, 2017; Karcıoğlu and Gürer, 2019; Pace et al., 2019a; Godio and Santilano, 2018) and magnetic data (e.g., Essa and Elhussein 2018; Liu et al. 2018) and seismological data (e.g., Song et al. 2012). A detailed review on this topic can be found in Pace et al. (2021).

2.2 Pareto-optimal multi-objective particle swarm optimization

Multi-objective optimization, where more than one objective function is optimized, leads to trade-off solutions between competing objectives and not to a single best solution as in single-objective PSO. Multi-objective optimization is defined to obtain the model vector $\boldsymbol{x} = [x_1, x_2, x_3, \dots\ x_m]$ in a m-dimensional model space, while the objectives in the N-dimensional objective space $\Phi(\boldsymbol{x}) = [\Phi_1(x), \Phi_2(x),\ \Phi_3(x) \dots\ \Phi_N(x)]$ are optimized, simultaneously. The Pareto optimality approach is one of the most successful methods for finding a set of optimal solutions in the feasible search space, as shown schematically in Figure 2. According to Pareto optimality approach, we say that x_a dominates x_b if and only if $\Phi_k(\boldsymbol{x}_a) \leq \Phi_k(\boldsymbol{x}_b), k = 1, \dots., N$, where N is the dimension of the objective function. We say that x_a is non-dominated and $\Phi(\boldsymbol{x}_a)$ is a non-dominated solution set if there does not exist the condition that $\Phi(\boldsymbol{x}_c) < \Phi(\boldsymbol{x}_a)$, where $\boldsymbol{x}_c$ denotes all possible model vectors. We also say that $\boldsymbol{x}_a$ is Pareto-optimal (Figure 2a), and $\Phi(\boldsymbol{x}_a)$ is Pareto front or Pareto-optimal set (henceforth will be referred as P^*) illustrated in Figure 2b. This indicates the trade-off solutions that conflict with each other in the objective function space, when $\boldsymbol{x}_a \in \mathcal{F}$ (feasible region as ilustrated in Figure 2a) is non-dominated. The solution closest to the origin (0,0) can be considered as the Pareto-optimum solution (POS), within the P^*(Baumgartner et al., 2004; Büyük, 2021, 2024;

Reyes-Sierra and Coello Coello, 2006; Schnaidt et al., 2018). Although Pareto optimality is widely used for multi-objective optimization in engineering problems, only a few researchers such as Büyük et al. (2020); Pace et al. (2019b); Schnaidt et al. (2018); Akca et al. (2014); Tronicke et al. (2011); Dal Moro (2010); Kozlovskaya et al. (2007); Paasche and Tronicke (2007); Moorkamp et al. (2010); integrated global optimization algorithms with the Pareto optimality approach to jointly invert various geophysical data.

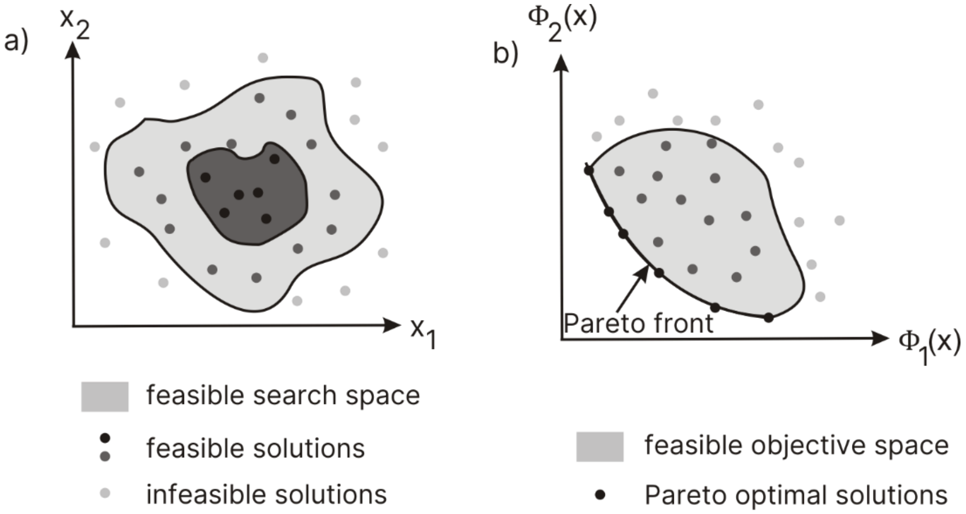

Figure 2: Illustration of the two-dimensional feasible model space with realizable solutions within meaningful search space, and infeasible solutions (a), solutions projected onto two-dimensional objective function space with Pareto optimal solution set having solutions that are non-dominated by the others in the feasible solutions, modified from Kumar and Minz (2014) and Büyük (2021)

3 Description of Synthetic Data Examples

Figure 3a shows synthetic apparent resistivity data for twenty periods from 10^{-2} to 10^{3} s obtained from a synthetic 1-D electrical resistivity model (Figure 3c) having low resistivities around 10 km depth. Figure 3b also shows the synthetic RWD curve for twenty periods from 5 to 20 s obtained from the 1-D velocity model (Figure 3d) that mimics the physical change of the 1-D electrical resistivity model. This example indicates compatible models showing low resistivities versus low velocities or vice versa in each layer without scaling. We therefore refer to these models as compatible models following Moorkamp et al. (2010). In the low resistivity layer (Figure 3c), the decrement of resistivity is kept wider than the seismic velocity, so that the presented method can determine physical variations on very large different scales. Figure 3e and Figure 3f show the apparent resistivity and RWD data, obtained from the synthetic resistivity-depth model having low resistivity layers (Figure 3g) and the velocity model (Figure 3h) which is insensitive to low resistivity layers as in the compatible model. The difference in the incompatible models is that the decrement of resistivity in the layer is kept lower than in the compatible model by referring to the insensitivity of the seismic velocity. In contrast to the compatible models in Figure 3c and Figure 3d, this example shows incompatible parameters in the corresponding layers, which we refer to as incompatible models. In order to exploit from common sensitivity of the data sets, we preferred to use apparent resistivity instead of phase data. This is because apparent resistivity data are sensitive to the absolute average resistivity of the subsurface material at the penetrated depth, similar to how RWD data are sensitive to shear wave velocity (Scherbaum et al., 2003; Simpson and Bahr, 2005).

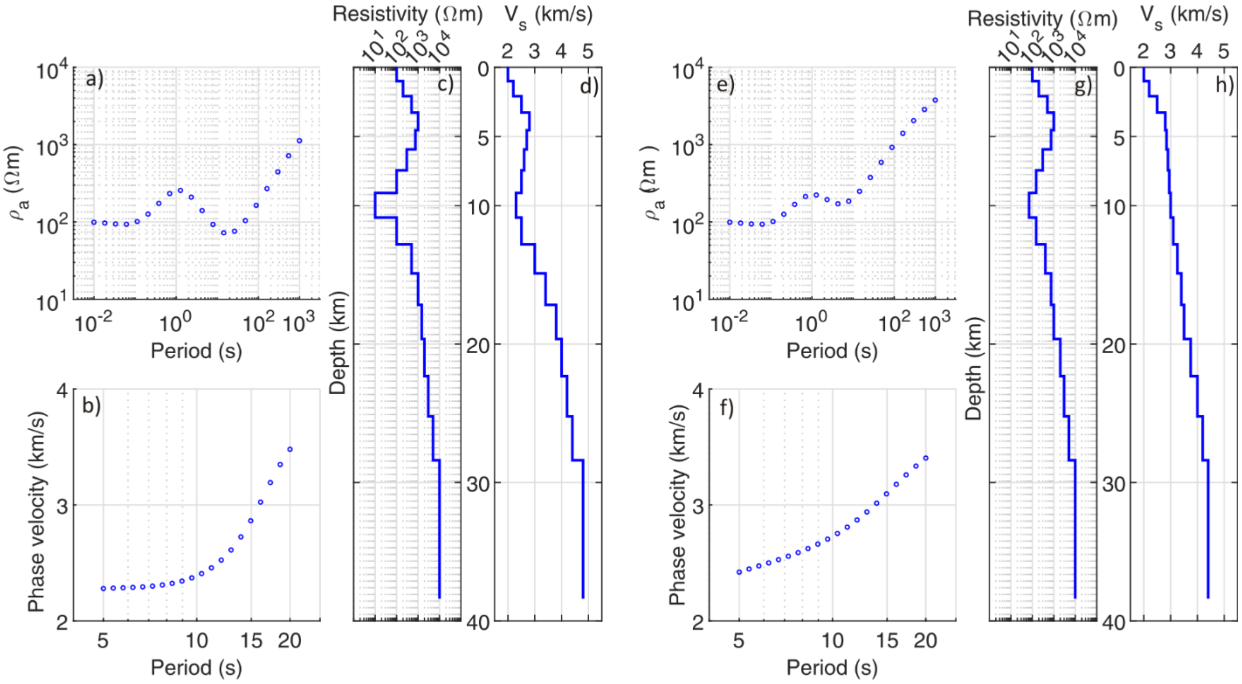

Figure 3: Synthetic apparent resistivities (a) and RWD curve (b) generated from the resistivity-depth (c) and the velocity-depth model (d), respectively, indicating compatible case. Synthetic apparent resistivities (e) and RWD curve (f) generated from the resistivity-depth (g) and the velocity-depth model (h), respectively, indicating incompatible case.

Synthetic apparent resistivities that are calculated using the effective impedance tensor proposed by Berdichevsky et al. (1989), were generated using Wait (1954) recursion formula based on one-dimensional magnetotelluric responses. The dispersion curves for the fundamental mode were generated using the open-source software package *SESARRAY* developed as part of the SESAME European Project presented by Bard (2000). These algorithms were used to generate the forward model response for Pareto-MOPSO.

4 Description of the Field Datasets

4.1 Rayleigh wave dispersion curves from earthquake data

In this study, we applied the two-station method, which uses a technique described by McMechan and Yedlin (1981) to obtain the inter-station phase velocities using the codes provided by Hermann (2002). In this technique, the entire wavefield of the data is transferred to the slowness-frequency domain (p-ω) to pick the RWD curve directly, which involves a linear transformation of the slant stack followed by a 1D Fourier transform. We used broadband data from an earthquake with a magnitude of Mw = 6.5 occurred in Italy on 30 October 2016. The earthquake is approximately 1200 km away from the study area, which is located in the south-eastern part of the Biga Peninsula between Ayvacık and Edremit bay in Çanakkale province, Türkiye. The data of this earthquake from these permanent stations are extracted from the waveform database of the Disaster and Emergency Management Presidency (AFAD). Before applying the two-station method, we first removed the mean, trend and instrument response from the earthquake recordings. This method also requires the two stations to be aligned on a path with the epicenter of the earthquake. We found three paths from station BOZC to stations BUHA, STEP and DEMI (hereafter referred to as BOZC_paths), where the azimuthal difference between the source to station-1 and the source to station-2 is less than 2 degrees. We also found for station ECEA to stations STEP and DEMI (hereafter referred to as ECEA_paths) with an azimuthal difference of less than 7 degrees.

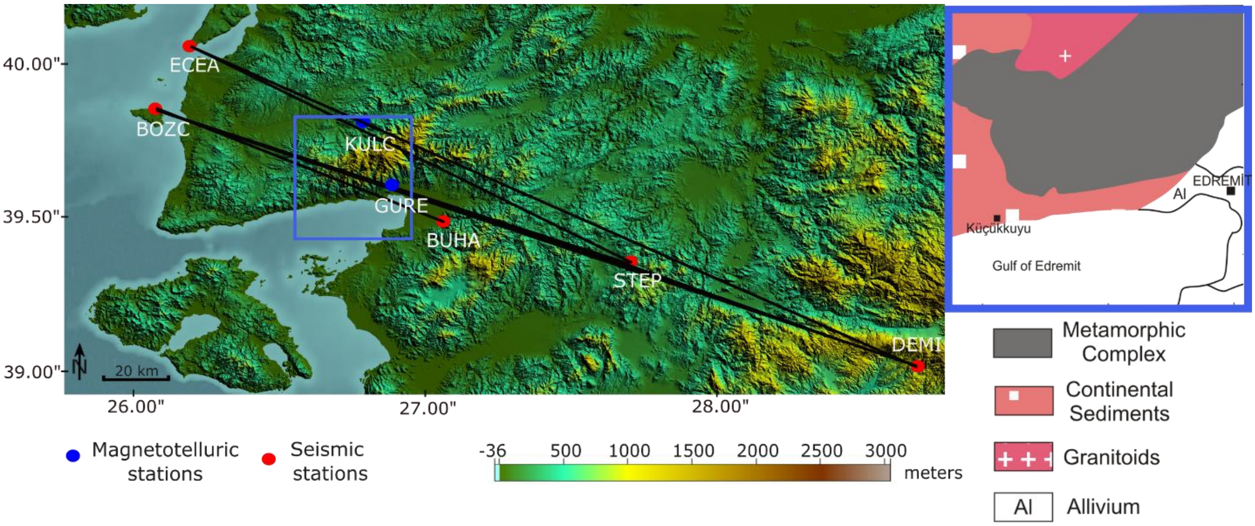

Figure 4: Magnetotelluric and seismic stations over a topographic map obtained from Shuttle Radar Topography Mission (SRTM) data. Black lines indicate the seismic station pairs used to obtain RWD curves. The blue rectangular area shows the geological base map of the southeastern Biga Peninsula reconstructed from Beccaletto (2003) **and** Yilmaz et al. (2001)**.**

4.2 Magnetotelluric data

MT is a passive electromagnetic method that enables to determine the subsurface electrical resistivity $\rho(\Omega m)$ by measuring the natural variations of the wide spectrum of electric and magnetic fields induced by natural sources (e.g., solar wind, lightning) (Chave and Jones, 2012; Simpson and Bahr, 2005). If we consider that the Earth as a transfer function that provides a predictable output in response to an input, the output is the time-varying electric field in response to the time-varying magnetic field in the MT method. (Buttkus, 2000). The MT method operates over a wide period range, typically from 10^{-5} to 10^{5} seconds and allows the investigation of different depths from the near-surface to the upper mantle (Chave and Jones, 2012; Romano et al., 2018). The source of the electromagnetic waves are the magnetic fields, which change internally or externally. The components of the internal source are the dynamo motion of the outer core and the permanent magnetization of rocks, while the external sources are the atmosphere and the magnetosphere. However, since the change of the internal source is very slow, external sources are used as electromagnetic sources in the MT method (Naidu, 2012; Simpson and Bahr, 2005; Vozoff, 1990). Signals with a frequency of more than 1 s in external sources originate from the magnetosphere. In MT studies, the source of EM waves with a frequency of less than 1 s is meteorological activity such as lightning, which propagates around the world (Chave and Jones, 2012; Simpson and Bahr, 2005)

We measured MT data at GURE and KULC stations shown in Figure 4 due to their positions, which are on the BOZC_paths and ECEA_paths, respectively. The MT field data were obtained using a *Metronix ADU-07e* receiver unit. Sampling rates of 65536, 16384, 4096, 1024, 512 and 128 Hz were used to record electromagnetic time series with durations of 2, 4, 8, 16, 32 and 2880 minutes, corresponding to 48 hours at each MT station. The fundamental principle of the MT method is the measurement of the impedance tensor, which relates the electric and magnetic fields on the Earth surface. This tensor is crucial for deriving the apparent resistivity of subsurface materials, which is a key indicator of geological features. (Chave and Jones, 2012; Simpson and Bahr, 2005; Smirnov, 2003). Conversion of time series to spectral analysis allows for the extraction of the impedance tensor, which is essential for deriving the apparent resistivity and phase information (Buttkus, 2000). The software package ProcMT (Friedrichs, 2007) was used to perform most of the data processing steps, namely time windowing, fast Fourier transform (FFT), power and cross spectra and stacking to obtain apparent resistivities and phase angles from the impedance tensor in the data set. To obtain the spectral ratios of the electric and magnetic fields, the FFT of the portion of the data set from a simultaneously advancing time window was used repeatedly to obtain a stacked power-, and cross-spectra.

5 Site Description

The southeastern Biga Peninsula, with its complex structural features of tectonic and magmatic origin, has received considerable attention in several studies (e.g., McKenzie, 1978; Dewey and Şengör, 1979; Taymaz et al., 1991; Okay et al., 1996; Karacık and Yılmaz, 1998; Altunkaynak et al., 2012). As shown in Figure 4, the simplified map describes the geology of the study site with outcrops of a combination of continental and oceanic crustal units corresponding to metamorphic, magmatic and sedimentary rocks. The magmatic process initiated with the complete closure of the Neo-Tethys Ocean subducted into the Sakarya Zone consisting of the Kazdağ metamorphic complex and formed by the subsequent interaction between crust and mantle (Okay and Satir, 2000; Şengün et al., 2011). After complete closure, a continental collision in N-S compression led to partial melting of the lithospheric mantle (Aldanmaz et al., 2000; Altunkaynak and Genç, 2008; Okay et al., 1996; Yilmaz, 1990). The Kazdağ metamorphic complex has a dome-shaped structure enclosed by a marble-rich sequence (Beccaletto, 2003). The N-S extensional regime occurred after the N-S compressional regime from the early Miocene to the late Pliocene triggered volcanic activities (Aslan et al., 2017; Yilmaz et al., 2001). The phases of volcanism are divided into two: 1) The N-S compressional regime, the result of continental collision, produced andesitic lavas with calc-alkaline characteristics through partial melting (Altunkaynak and Genç, 2008; Yilmaz et al., 2001). The second group of volcanics with potassium-rich basaltic volcanics formed during the extensional regime (Altunkaynak and Genç, 2008; Fytikas et al., 1976; McKenzie and Yılmaz, 1991; Yilmaz, 1990). The sedimentary rocks from the Miocene to the Pliocene were deposited as cover units over the ignimbrites, the last product of volcanism (Seyitoğlu and Scott, 1991). Differently aged continental shallow sediments unconformably cover the metamorphosed units of the Kazdağ metamorphic complex (Altıner et al., 1991).

6 Description of the Parameter Settings

6.1 Model parameters and misfit functions

The misfit, $\phi_{MT}(\boldsymbol{d},\boldsymbol{m})$, between the vectors of magnetotelluric data ($\boldsymbol{d}$) and model response ($\boldsymbol{m}$), yielding normalized root mean square error (NRMSE) was calculated using:

$$\Phi_{MT}(\boldsymbol{d},\boldsymbol{m}) = \left(\left[\frac{1}{n}\sum_{i=1}^{n}\left(\frac{\rho_i^{obs}-\rho_i^{cal}}{\Delta_{\rho,i}}\right)^2\right]^{1/2}\right) \tag{3}$$

where n is the number of observations, $\rho_{a,i}^{obs}$ and $\rho_{a,i}^{cal}$ are the observed and calculated apparent resistivities ($\log_{10} ohm.m$), respectively. $\Delta_{\rho a,i}$ is the standard deviations of the observed apparent resistivities. Data misfit term of RWD data was also calculated using as NRMSE as:

$$\Phi_{RWD}(\boldsymbol{d},\boldsymbol{m}) = \left(\left[\frac{1}{n}\sum_{i=1}^{n}\left(\frac{V_{p,i}^{obs}-V_{p,i}^{cal}}{\Delta_{Vp,i}}\right)^2\right]^{1/2}\right) \tag{4}$$

where n is the number of observations, $V_{p,i}^{obs}$ and $V_{p,i}^{cal}$ are the observed and calculated phase velocities (km/s), respectively. $\Delta_{Vp,i}$ is the standard deviations of the observed phase velocities. Equation 3 and 4 were used for both synthetic tests and field data to ensure consistency when comparing solutions.

Although the estimation of layer thicknesses could lead to a complicated solution (Siripunvaraporn et al., 2005), the layer thicknesses are also estimated by PSO in the modeling stage to couple the electrical resistivity and seismic velocity parameters in the corresponding layers. Therefore, coupling is provided by layer thicknesses estimated from the PSO algorithm rather than prescribed spatial locations. In this case, with a total of thirty-one model parameters, consisting of sixteen-layer physical parameters and fifteen-layer thicknesses, compared to twenty produced periods of both datasets, the inverse solution problem is an underdetermined problem that requires a regularization technique as one of the ways to overcome the sampling problem of swarm intelligence algorithms (Juan Luis Fernández Martínez et al. 2012; Godio and Santilano 2018; Pace et al. 2021). Since in this case we dealt with a high-dimensional model space that may have an ill-posed character, the solution sampling of the PSO was limited due to the curse of dimensionality (Curtis and Lomax, 2001;

Fernández Martínez et al., 2012). Although it was necessary to control the solution sampling with different types of regularization, we used a new method proposed by Büyük (2024) without the need for a subjective and iteration-dependent regularization parameter by adding a constraint term as a new axis to the objective function space. The constraint term Φ_c, was calculated by summing the numerical gradients of the electrical resistivity and seismic velocity parameters as follows:

$$\Phi_C(\boldsymbol{m}) = \left(\left[\frac{1}{n} \sum_{i=1}^{n} \left(\frac{\partial \boldsymbol{m}_{MT}}{\partial z} \right)^2 \right]^{1/2} + \left[\frac{1}{n} \sum_{i=1}^{n} \left(\frac{\partial \boldsymbol{m}_{RWD}}{\partial z} \right)^2 \right]^{1/2} \right) / 2 \tag{5}$$

where the units of $\partial \boldsymbol{m}_{MT}$ and $\partial \boldsymbol{m}_{RWD}$ are $\log_{10} \Omega m$ and km/s, respectively. This equation indicates an additional objective function term that constrains the change in physical parameters. As Equation 3 and Equation 4, this equation is the third term of the objective function and forms the third axis in the Pareto space. Therefore, independent minimizations are applied without the need for regularization parameters both in the misfit functions and in the model variation. The output of this term corresponds to the differences of the parameters in z-direction (depth). The parameter search space of these model parameters that should be restricted to ensure a feasible solution set, was defined in the range [1, 5] $\log_{10}\Omega m$ for resistivities, and [1.5, 5] km/s for S-wave velocities to cover realistic values in the crust. The P-wave velocities and densities were calculated using the equations given by Berteussen (1977) as typically observed in the crustal zone.

6.2 MOPSO and Pareto optimality parameters

We used velocity limiting approach proposed by Fan and Shi (2001) to constrain the velocity of particles that tend to explode to large values if the particle is far from the global and local best position. This approach limits the particle velocities as follows: $V_{max} = +U$ and $V_{min} = -U$, where $U = (m_{max} - m_{min})/N$. m_{max} and m_{min} are the 5 and 1 $\log_{10}\Omega m$ for MT modeling and 5 and 1.5 km/s for RWD modeling as the defined parameter search space. N is the interval number, which was set to 10. We used modified velocity equation of the Equation 1, proposed by Clerc and Kennedy (2002) to obtain solutions without trapping a local minimum due to premature convergence, as defined below:

$$\boldsymbol{V}_i^{k+1} = \chi\left[\boldsymbol{V}_i^k + c_1\gamma_1 \otimes \left(\boldsymbol{x}_{pbest,i} - \boldsymbol{x}_i^k\right) + c_2\gamma_2 \otimes \left(\boldsymbol{x}_{gbest} - \boldsymbol{x}_i^k\right)\right] \tag{6}$$

where, χ is the constriction factor expressed as: $\chi = 2/(k - 2 + \sqrt{k^2 - 4k})$ under the condition that $k = c_1 + c_2 > 4$. Therefore, we used c_1 and c_2 as 2.05, i.e., $k = 4.1$ and $\chi = 0.7298$. The number of particles was set to 5-fold the number of model parameters (e.g. 155 particles for total of thirty-one model parameters when modeling one dataset). Iteration was terminated at 1000 iterations for both synthetic and field data sets as one way of limiting the maximum number of iterations (Reyes-Sierra and Coello Coello, 2006) and ten experimental solutions were generated repeatedly and the final Pareto-optimum model which misfit was closest to the utopia point (0,0) was selected.

In the Pareto optimality approach, objective function space is divided into hyper-rectangles, to each of which control solutions are added (Coello Coello et al., 2004; Coxeter, 1973). One-tenth of the number of particles was defined as the number of hyper-rectangles for each objective function. The roulette wheel selection, one of the scheme theorems proposed by Coello Coello et al. (2004), which is based on the rational division of the segments of the wheel according to the number of non-dominated solutions in each of the hyper-rectangles, was used to select a leader for MOPSO. According to this theorem, the ratio decides the selection probability (Ps) of an individual hyper-rectangle as follows: $Ps(k) = n_k/\sum_{i=1}^{N} n_i\,;\quad i = 1,2, \dots\dots, N$, where, N is the number of hyper-rectangles with non-dominated solutions n_k is the number of non-dominated solutions of the kth hyper-rectangle (Rao, 2009). A leader is randomly determined from the selected hyper-rectangle.

7 Results and Discussions

7.1 Synthetic data examples

7.1.1 Compatible models

Figure 5a,b and 6a,b show the noise-free and %15 Gaussian noise added outputs of the compatible models, which agree very well with the synthetically generated observations. Figure 5c and Figure 6c show the objective function space that requires the minimization of the objective function terms of the *POS* and the P^*. Figure 5d,e and 6d,e show the resistivity-depth and velocity-depth models of the synthetic model, the model of the *POS* (*PO*-model) and the mean model obtained from the mean of the estimated parameters of the P^* (mP^*-model). These models strikingly highlight how many different models are structurally constrained to fit the curves produced. In this study, we analyzed the *PO*-model and the mP^*-model to obtain the best and the most reasonable models between different models. Although the *PO*-model and mP^*-model are compatible in each layer and mimic the synthetic model in the noise-free case (shown in Figure 5d,e), we found that the *PO*-model is incompatible at several layers in the noisy case and have different physical directions from the both synthetic and the mP^*-model in the 4th layer of the resistivity-depth model, and 8th layer of the velocity-depth model, as shown in rectangular shape in Figure 6d,e. Therefore, we decided to obtain the posteriori probability density function (PDF), a well-known procedure for examining the estimated parameters, as shown in Figure 6f, g. In these figures, significant differences between the *PO*-model and the mP^*-model can be seen at the aforementioned layers. The PDFs of the estimated parameter in the mP^*-model are clearly both closer to the real model, and have the highest number of repetitions compared to the parameter in the *PO*-model. On the other hand, the estimated parameter of the MT solution appears to be clearly resolvable compared to the RWD solution. In fact, seismic velocities and electrical resistivity are generally represented by the properties of large volumes of rock masses, but since even small fractions of conductive material can determine the bulk resistivity (Moorkamp et al., 2010; Simpson and Bahr, 2005). This reason may cause the resistivity parameter to approach a singular value, while the seismic velocity has a wide distribution on the PDF. Although the obtained lowest seismic velocity layer is close to the real model, it seems that the exact real value in the relatively sharp lowest resistivity layer cannot be determined in the resistivity model. The most important factor here is that the models with smooth transitions are promoted by adding the regularization term of the objective function into the Pareto space. However, the obtained resistivity model successfully mimics the sharp variation of the low resistivity layer of the synthetic model.

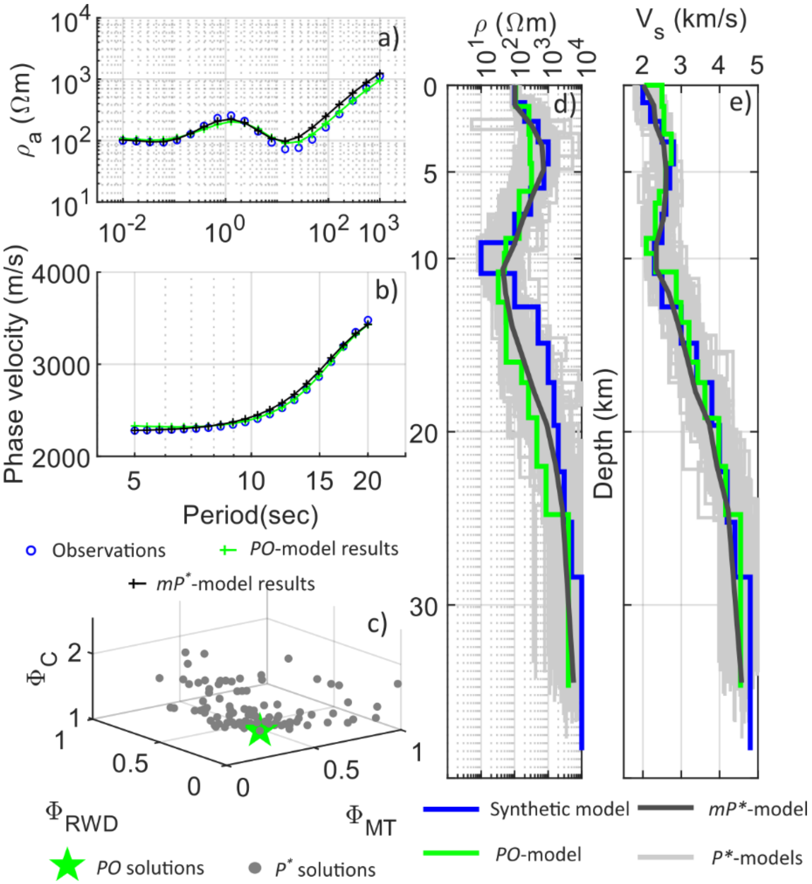

335 **Figure 5: Results for noise-free data from compatible models. The fit between apparent resistivities (a), and phase velocities (b); objective function space (c) indicates POS and P^*; Resistivity-depth (d) and velocity-depth (e) synthetic model, PO-model and mP*-model obtained from Pareto-front models indicating different structural couplings.**

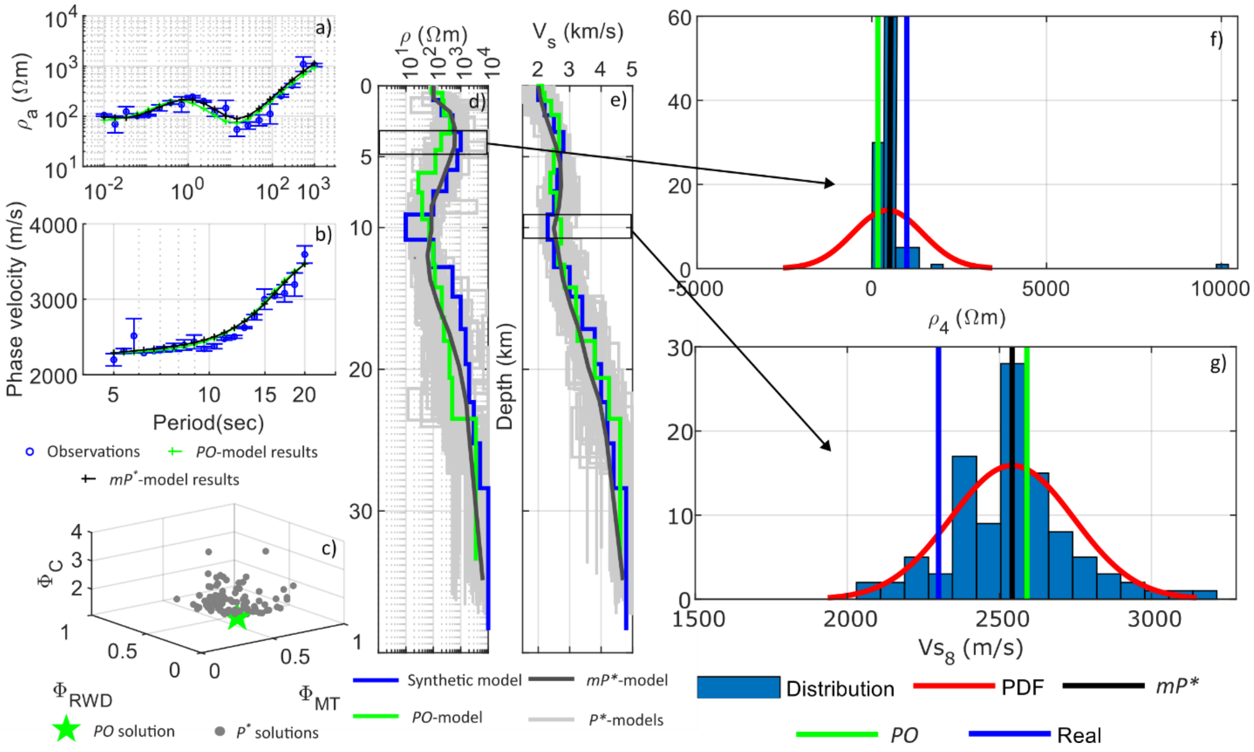

Figure 6: Results for noisy data from compatible models. The fit between apparent resistivities (a), and phase velocities (b); objective function space (c) indicates POS and P^*. Resistivity-depth (d) and velocity-depth (e) synthetic model, PO-model, mP*-model and P* showing different structural couplings. Posteriori PDF of the estimated resistivity (f) and seismic velocity (g) parameters indicating incompatibility in the layers shown in a rectangular area of the synthetic model, PO-model and the mP*-model.

As can be seen in Figure 5c, P^* solutions have an almost symmetric shape which means that the MT objective function cannot be further minimized without maximizing the RWD objective function and vice versa. However, Figure 6c shows that the clustered solutions of the P^* deviate slightly in the direction of the MT objective function axis. This deviation shows that seismic velocity parameters are very sensitive the noise condition, resulting in a high number of non-unique solutions that satisfy the RWD data misfit, as noted by Kozlovskaya et al. (2007) and Dal Moro (2010).

7.1.2 Incompatible models

Figure 7a,b and 8a,b show the outputs of the incompatible models (noisy and noise-free data), which fit the observed data well. Figure 7c and Figure 8c show the objective function space that requires the minimization of the objective function terms of the *POS* and the P^*. Apart from the Figure 7c, Figure 8c shows a deviation of P^* towards the MT objective function, indicating a high sensitivity of the seismic velocity parameter to noise condition compared to the electrical resistivity parameter, leading to high non-unique solutions, as similar to the results of the noise-added compatible models.

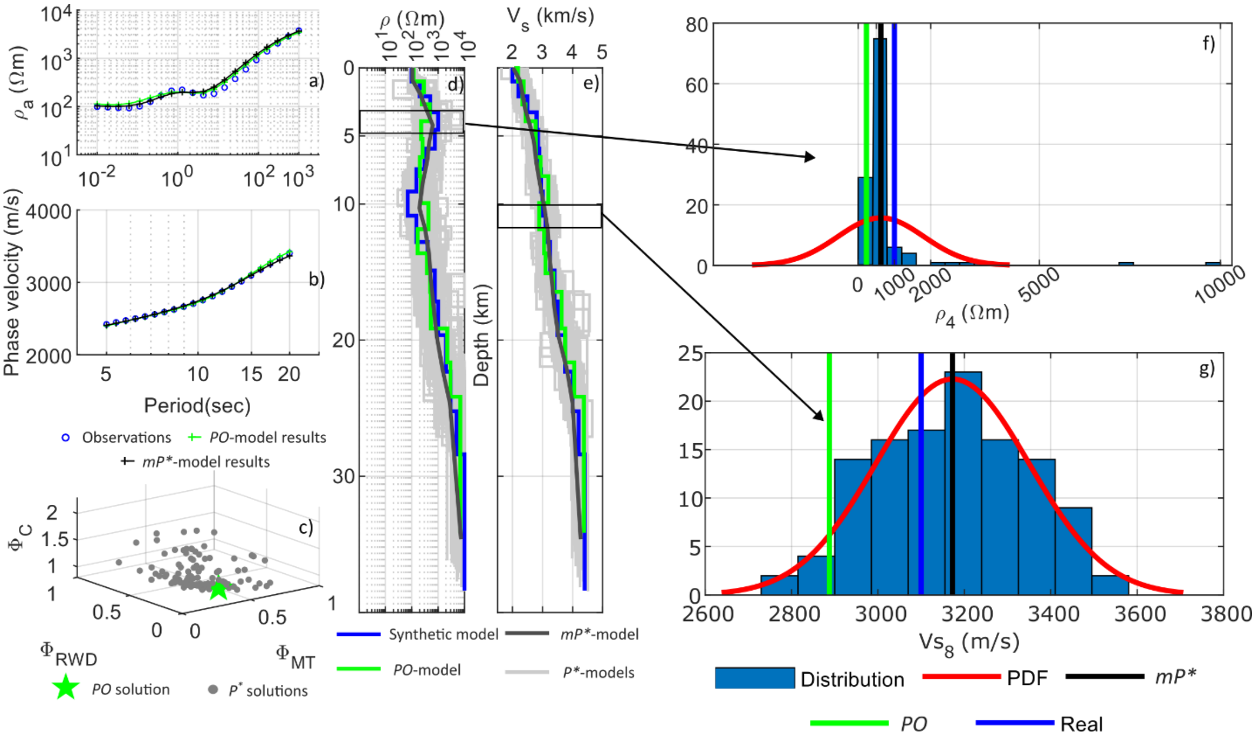

Figure 7: Results for noise-free data from incompatible models. The fit between apparent resistivities (a), and phase velocities (b); objective function space (c) indicates POS and P^*. Resistivity-depth (d) and velocity-depth (e) synthetic model, PO-model, mP*-model and P* showing different structural couplings. Posteriori PDF of the estimated resistivity (f) and seismic velocity (g) parameters indicating incompatibility in the layers shown in a rectangular area of the synthetic model, PO-model and the mP*-model.

Figure 7d,e and 8d,e show the resistivity-depth and velocity-depth models of the synthetic model, the *PO*-model and mP^*-model. Although the obtained models are clearly comparable to the synthetic model, we also examined the PDFs of the physical parameters of the synthetic model, *PO*-model and mP^*-model having different physical directions, as shown in Figure 7d,e and Figure 8d,e in a rectangular shape. In both cases (noisy and noise-free), the parameters obtained from the mean model are both closer to the real value and have a higher number of repetitions than those obtained from the *PO*-model, just as in the compatible model with noisy data. These results clearly identify that when a mP^*-model changes in a different direction compared to the *PO*-model, the physical parameter of the mP^*-model gives the same physical direction as the real model and is estimated to a value closer to the real model parameter. We have therefore opted for the mP^*-model when in modelling field data, considering that the estimated parameter of the *PO*-model may lead to misinterpretations. On the other hand, compared to previous (noisy compatible and noiseless incompatible) resistivity parameters, the PDFs of the estimated parameters of the MT solution seem to have a slightly wide distribution. These results indicate that the solution of the resistivity-depth model appears to be more complicated and it may be difficult to obtain a singular value when the noisy incompatible seismic model is jointly inverted.

https://doi.org/10.5194/egusphere-2025-4698
Preprint. Discussion started: 26 September 2025

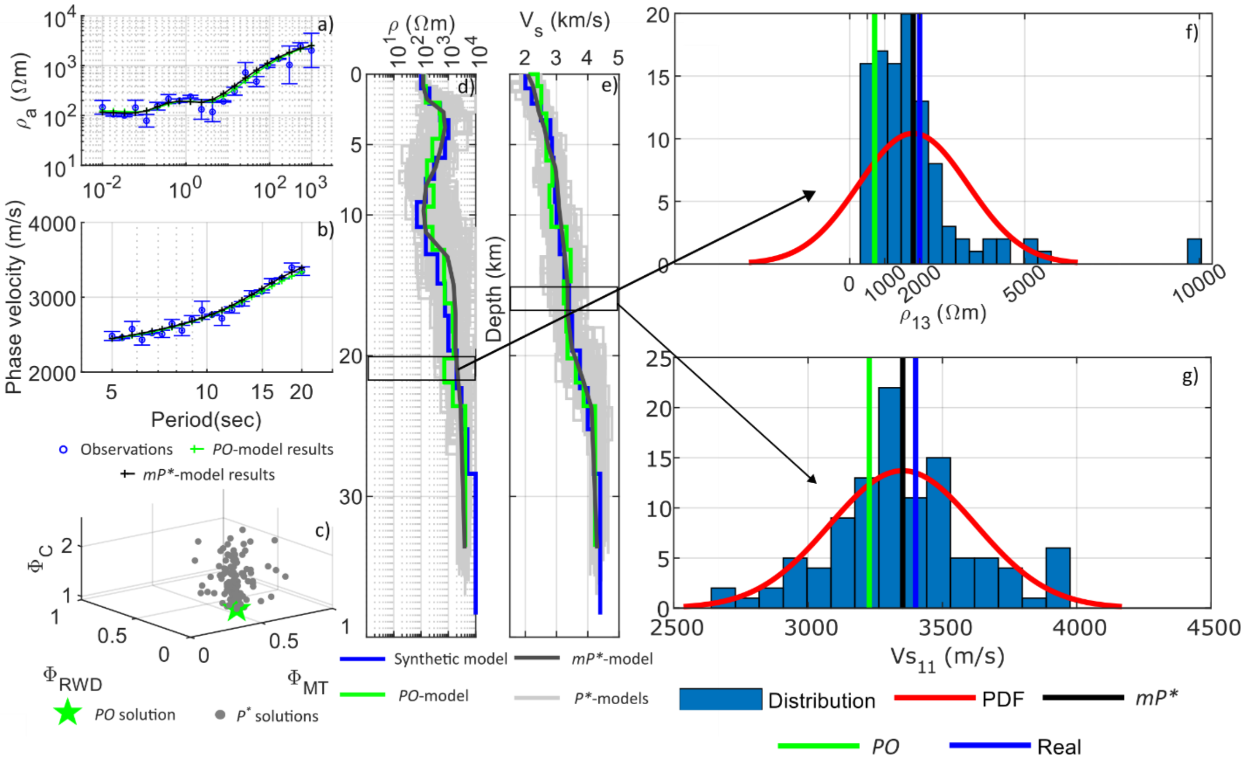

Figure 8: Results for noisy data from incompatible models. The fit between apparent resistivities (a), and phase velocities (b); objective function space (c) indicates POS and P^*. Resistivity-depth (d) and velocity-depth (e) synthetic model, PO-model, mP*-model and P* showing different structural couplings. Posteriori PDF of the estimated resistivity (f) and seismic velocity (g) parameters indicating incompatibility in the layers shown in a rectangular area of the synthetic model, PO-model and the mP*-model.

7.2 Field data

Figure 9 shows the phase velocity dispersion curves obtained from the pairs of BOZC_paths and ECEA_paths, as well as the combined curve that best represents the phase velocities of the crustal structure along the paths between the stations using the analysis of Özalaybey et al. (2011) . The period range was between 8 and 60 seconds, but we used 8 to 25 seconds for modeling to cover realistic values in the crust. The phase velocity curves indicate a crustal structure as the seismic velocities increase with increasing period, but possible low velocity structures can be identified as a result of the modelling phase. Figure 10 shows the apparent resistivities, phase angles and ϕ_{min} angles of the phase tensor from the GURE and KULC stations located over the BOZC_paths and ECEA_paths, respectively. The apparent resistivity curves show a high resistivity in the first periods and a low resistivity above 1 s. The phase tensor, which is independent of galvanic distortion compared to the impedance tensor (Hill et al., 2009), also shows a spatial variation from low to high phase angles, indicating high to low resistivities, as noted by Garcia and Diaz (2016) and Heise et al. (2008). However, continuous resistivity-depth models can be clearly verified by the joint inversion of the datasets. The lowest period of 0.1 seconds of the data seems to be distorted, which is probably due to the lack of processing of the remote reference or other reasons. However, these periods can be ignored to avoid the effects of the shallow layers in order to investigate the crustal structure of the Earth model. Therefore, except for the lowest periods, we used apparent resistivity data with periods longer than 0.1 seconds for modeling.

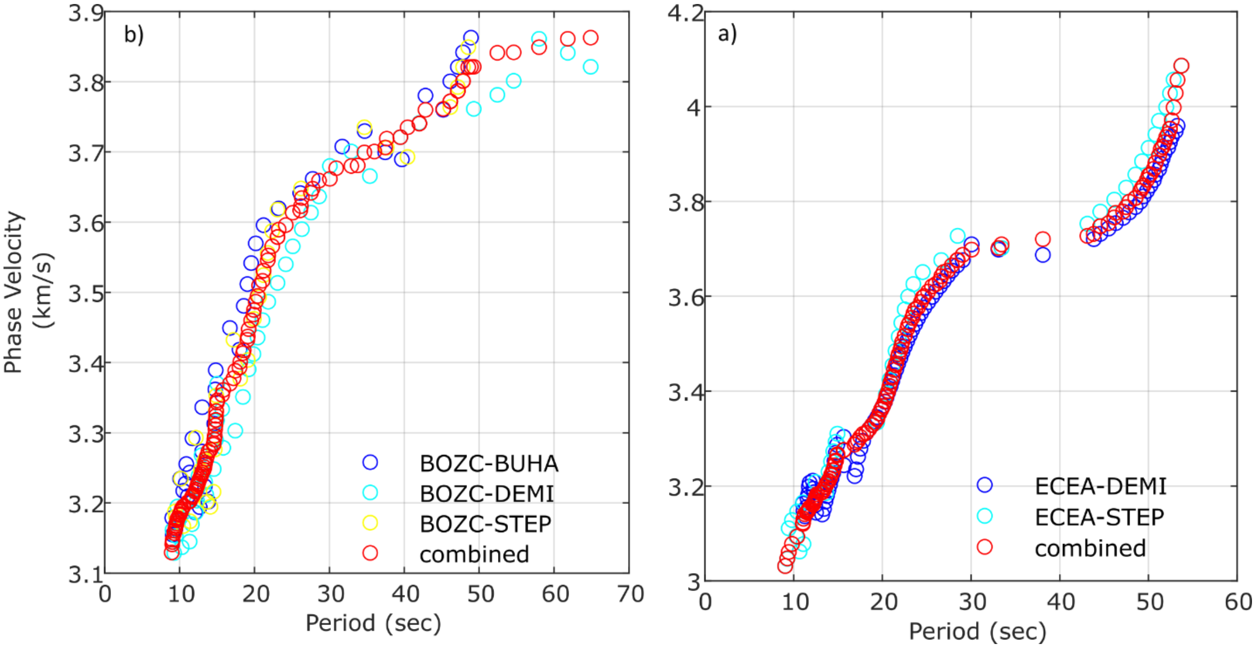

Figure 9: Measurements of an individual Rayleigh-wave dispersion curve obtained from BOZC_paths (a) and ECEA_paths (b) from an earthquake with a magnitude of Mw = 6.5 occurred in Italy on 30 October 2016.

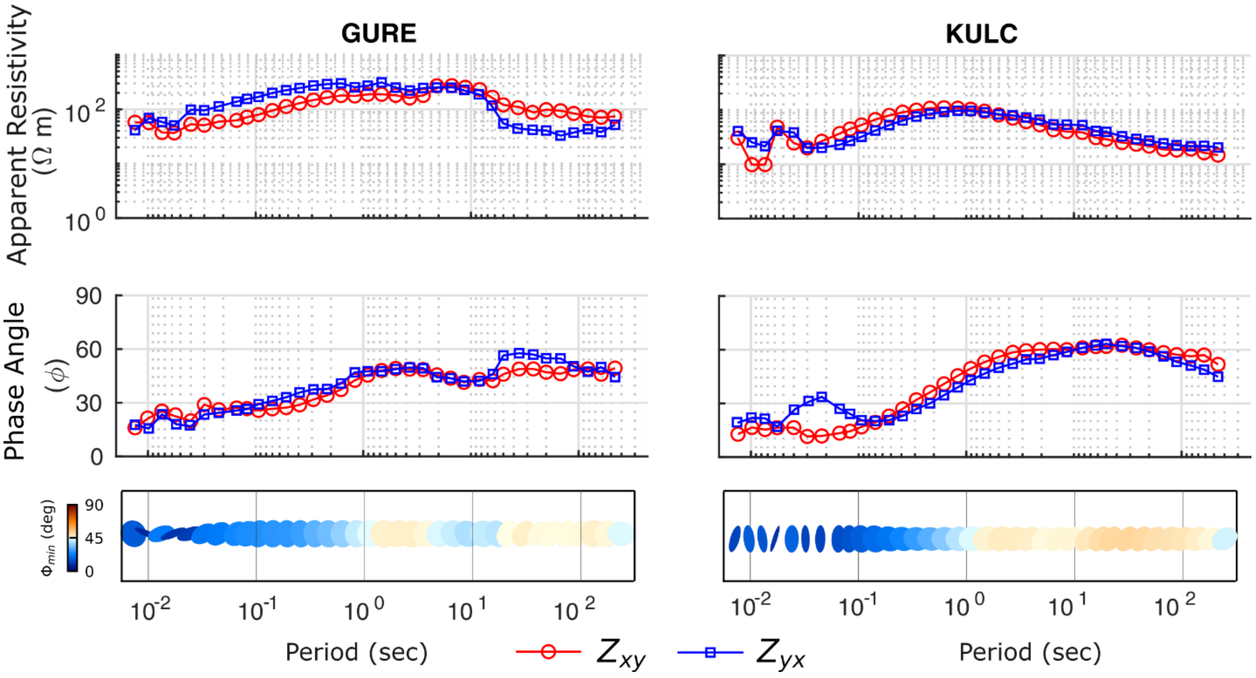

Figure 10: Measurements of individual apparent resistivities, phase angles and phase tensor $\boldsymbol{\phi_{min}}$ angles of GURE station over the BOZC_paths (left) and KULC station over the ECEA_paths (right).

Figure 11 and Figure 12 show the results of the crustal model obtained from the joint modeling of the MT and RWD data from the GURE station and BOZC_paths (henceforth will be referred as GB_p), and KULC station and ECEA_paths (henceforth will be referred as KE_p), respectively. Figure 11 a and Figure 12a show the apparent resistivity curve; Figure 11 b and Figure 12b show the phase velocity curve obtained from the *mP**-model that are well fitted to the observed data. Although, MT data of GURE station have a higher noise compared to MT data of KULC station, an agreement between the observed data and the model responses appears to be reasonably accurate and satisfactory within the standard deviation. Figure 11 c and Figure 12c show the objective function space that requires the minimization of the objective function terms of the P^*. Unlike the distribution of P^* in the objective function space of KE_p, a high noise component of the GB_p could be responsible for deviation of P^* to RWD axis that indicates a high non-unique solution in MT model.

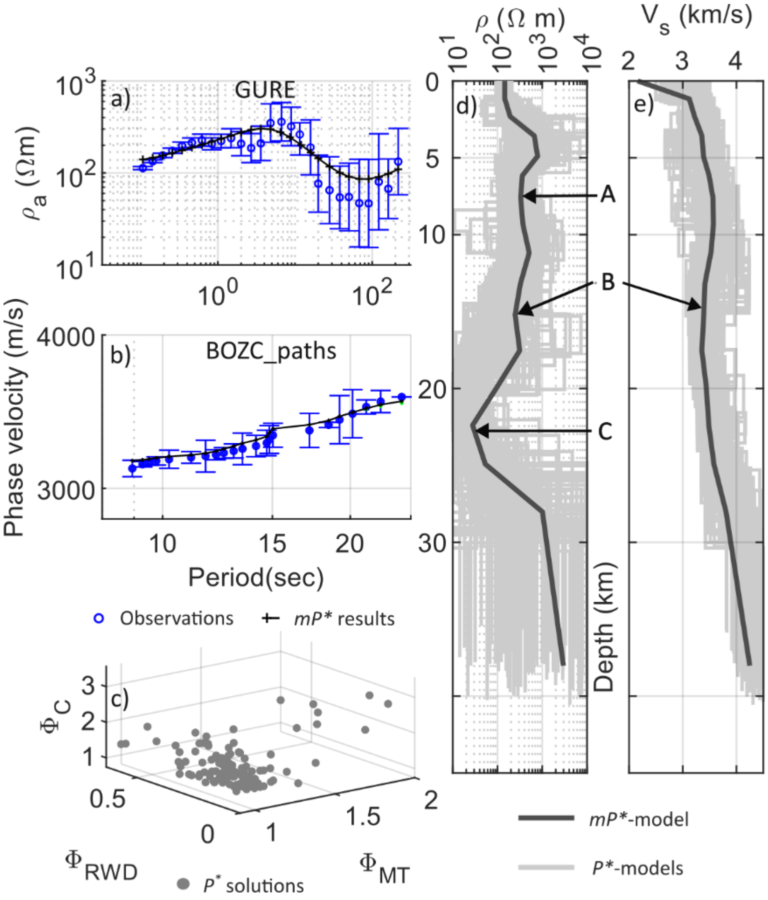

Figure 11: Results for GB_p. The fit between apparent resistivities (a), and phase velocities (b); objective function space (c) indicates $\boldsymbol{P^*}$. Resistivity-depth (d) and velocity-depth (e) models from *mP-model and $\boldsymbol{P^*}$.**

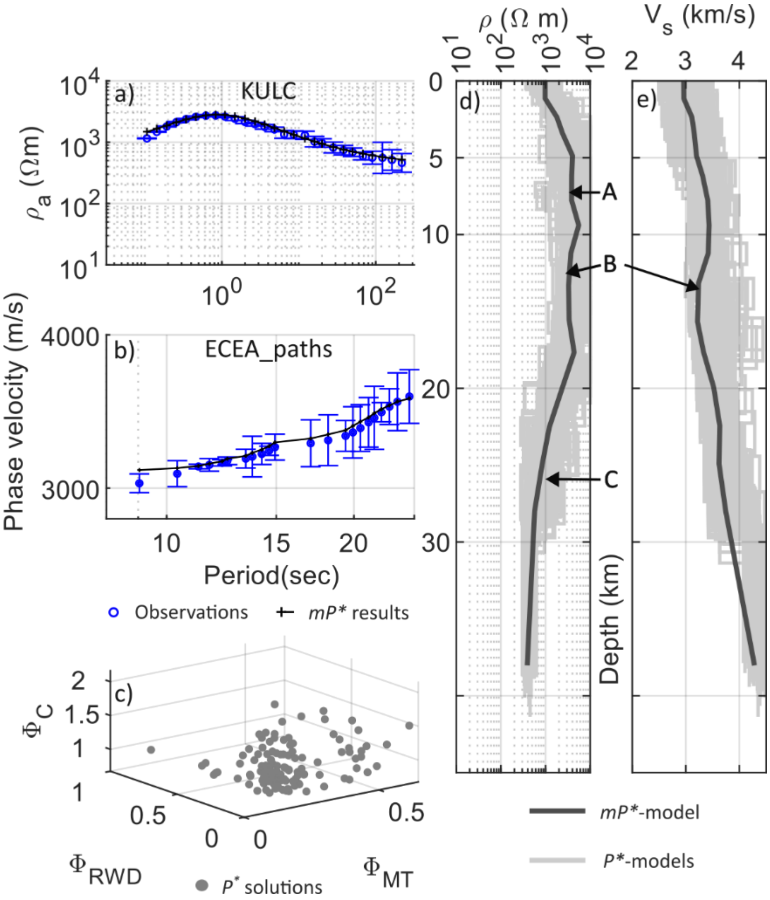

Figure 12: Results for KE_p. The fit between apparent resistivities (a), and phase velocities (b); objective function space (c) indicates P^*. Resistivity-depth (d) and velocity-depth (e) models from *mP-model and P^*.**

Figure 11d and Figure 12d show the obtained resistivity-depth; Figure 11e and Figure 12e show the obtained velocity-depth from *mP**-models. At both the GB_p and KE_p, an increasing resistivity and seismic velocity structure is observed extending up to 5 km from the surface. However, in contrast to the KE_p, the GB_p shows the influence of the continental sediments as the geological surface structure in which it is located, with a relatively low resistivity and velocity structure extending up to 1-2 km. At the GB_p and KE_p, shown as Region A in Figure 11d and Figure 12d, a low resistivity structure is observed extending from 5 km to about 10 km with no remarkably change in seismic velocity in the same layers. This zone indicates an example of an incompatible model in which the seismic velocity almost does not change despite the conductive layers, due to different influence of the amount of volume rocks to bulk resistivity and seismic velocity, as indicated by Moorkamp et al. (2010). On the other hand, this observation can be attributed to MT method is more sensitive to the decrease in resistivity than to the decrease in seismic velocity compared to the RWD method (Wu et al. 2018), as can be inferred from the velocity*thickness and resistivity*thickness relationship described by Moorkamp et al. (2013). There are many geothermal fields in the vicinity of the GURE station, and it is a possible indication that Zone A, which has a lower resistivity than the KULC station, is under the influence of volcanics that have undergone hydrothermal alteration. The volcanics present in the study area, which consist of andesitic lavas, are normally resistive. However, these volcanics may have a low resistivity due to the clay content as a result of alteration (Stanley et al., 1977).

The most remarkable result of the joint modelling is region B, where both seismic velocity and resistivity decrease. Normally, a low velocity and low resistivity structure in the crust indicate the presence of aqueous fluids (Eberhart-Phillips et al., 1995) or a change in Vp/Vs and attenuation (Okada et al., 2014). Moreover, a number of theoretical studies have found that elastic wave velocities gradually decrease with the existence of fluid and/or melt in the mid-to-lower crust (e.g., Nakajima et al. 2001; Takei 1998; Zhao, et al. 2002). Our results are consistent with one and the recent publication of Turunçtur et al. (2023), which indicate a low seismic velocity which extends from 10 km to about 15-16 km in the crustal structure of the southeastern part of the Biga Peninsula, as determined by seismic noise tomography. The possible source of Region B is the mantle-derived melt that emplaced the crust during outcropping. This is because system processes were triggered in the magma chambers in the study area that enabled the production of granitic magmas. The intrusion of mantle-derived magmatic rocks into the crust has created magma chambers and melting environments in the crust, known as MASH (melting, assimilation, storage, homogenization), as described by Hildreth and Moorbath (1988). While the magmatism process caused thermal weakening in the young orogenic crust, it accelerated the process of crustal expansion and outcrop in the crustal environment of the Biga Peninsula (Altunkaynak et al., 2012; Okay and Satir, 2000). Therefore, the low-resistivity and low-velocity zone is considered to be granitoid magma, which is an important indicator of granitoids formed by the simultaneous assimilation of upper and middle crustal rocks and fractional crystallization of melts from the mantle during magma ascent. However, one limitation of our research is that the models were not compared with well-logs or other geophysical studies that investigated the crust and/or mid-crust structures in the study area.

Region C with a low resistivity structure in both stations could indicate the low resistivity of the lower crustal zone suggested by Jones (2013). The dominant factor for the electrical resistivity in the lower crust is the presence and the interconnectedness of aqueous fluid, volumetric partial melt or grain boundary mineralization (Feucht et al., 2017). However, if aqueous fluids or partial melting could be the primary factor in the lower crust, a low seismic velocity could have been observed, as in region B. From this point of view, it can be assumed that mineralization is effective at the grain boundary in the lower crust. Because as Christensen and Mooney (1995) stated as a result of field and laboratory studies, the lower crust containing mafic granulite minerals alone does not cause a decrease in seismic velocity. According to Yang et al. (2012), the presence of granulites as the main structural mineral in the lower crust provides low resistivity and does not necessarily require the contribution of other low resistivity materials such as aqueous fluids, melts or graphite films to ensure this feature. However, it would not be a critical comment on the lower crust, considering that the poor performance of the lowermost layers and homogenous half-space contribute to the solution (Zhdanov 2018). Since both MT and RWD datasets have low sensitivity to the sharp Moho boundary that can be clearly observed in seismic velocity, it is difficult to interpret with the presented datasets. However, future receiver function studies on this topic are therefore recommended to obtain more reliable results for the lower crust.

Figure 13 and Figure 14 show the posteriori PDFs of the A, B and C regions for the GB_p and KE_p solutions, respectively. We used all physical parameters in each region obtained from the Pareto-optimal solution set to provide a comprehensive framework for assessing uncertainties associated with model parameters. We found that the peak values of the posterior PDFs for all model parameters converge to a singular value, indicating lower uncertainty. As expected, the distribution of the resistivity parameter is narrower than that of the seismic velocity, as in the synthetic analysis. This confirms the higher sensitivity of bulk resistivity to rock mass fraction compared to seismic velocity. We also performed a sensitivity analysis to understand how variations in the input parameters affect the responses of the resistivity depth and seismic velocity depth models. Our test follows the quantitative analysis given by (Garcia et al., 2015) to evaluate the quality of the data fit as follows: $\Phi(\%) = 100 \times (\Phi_n - \Phi_o)/\Phi_o$, where Φ_n is the new NRMSE of the perturbed model, Φ_o is the NRMSE of the final (preferred) model. If the $\Phi(\%)$ is positive, it means a deterioration of the data fit compared to the final model. Table 1 shows the results of the sensitivity tests performed by substituting final model with perturbed model defined by new model parameters in each region A, B and C. Considering the model parameters of the layers above each region, we used incremental model parameters if the final model had decreasing properties and vice versa. As can be seen inTable 1, slightly increased $\Phi(\%)$ is observed in each region of the models. These results highlight the deterioration in data fit after forward modelling of the perturbed models in each region. We would expect a higher $\Phi(\%)$ in region C, which is represented by more layers than regions A and B. These results indicate that region C is relatively less sensitive to the fit of the data. However, our results appear to be reliable models down to a depth of 20 km, including regions A and B.

Although one-dimensional modeling can be reliably performed in several studies by obtaining dispersion curves from earthquake data or long-term records (e.g., Lee et al., 2020; Gupta et al., 2023; Manakou et al., 2023), one-dimensional modeling of magnetotelluric data may be unsuitable if MT mode differences and /or elliptical phase tensors as partially observed about 10 seconds in Figure 10 (Simpson and Bahr, 2005, p.110). This points out the slightly effects of the high-dimensional structures on the data. However, we needed to use the one-dimensional resistivity-depth model to achieve structurally constraint with the velocity-depth model, which we believed could be reliably obtained. On the other hand, we used the effective impedance tensor of the data for the one-dimensional MT modeling as a starting point for more complex analyses. This allows us to identify key resistivity contrasts that may indicate different geological materials or fluid presence as indicated by Chave and Jones, (2012) and Tietze and Ritter (2013). Therefore, presented results provide only a rough overview of the crustal structure of southeastern Biga Peninsula. Since this study focuses on the practicality of Pareto-MOPSO on joint modeling MT and RWD data having different sensitivities, a detailed interpretation of crustal structure is outside the scope of this study utilizing with a few datasets joint modelled as one-dimensional. Nevertheless, the Pareto-MOPSO is suggested for 2D and 3D joint modelling of MT and RWD data, in which a number of model parameters is too large. We believe that this methodology indirectly allows for the reduction of constant forward computation in the model space by adding additional datasets to the data space. Therefore, this study is an encouragement for high-dimensional modelers using high computational capacity, even though it might be computationally intensive in such dimensions.

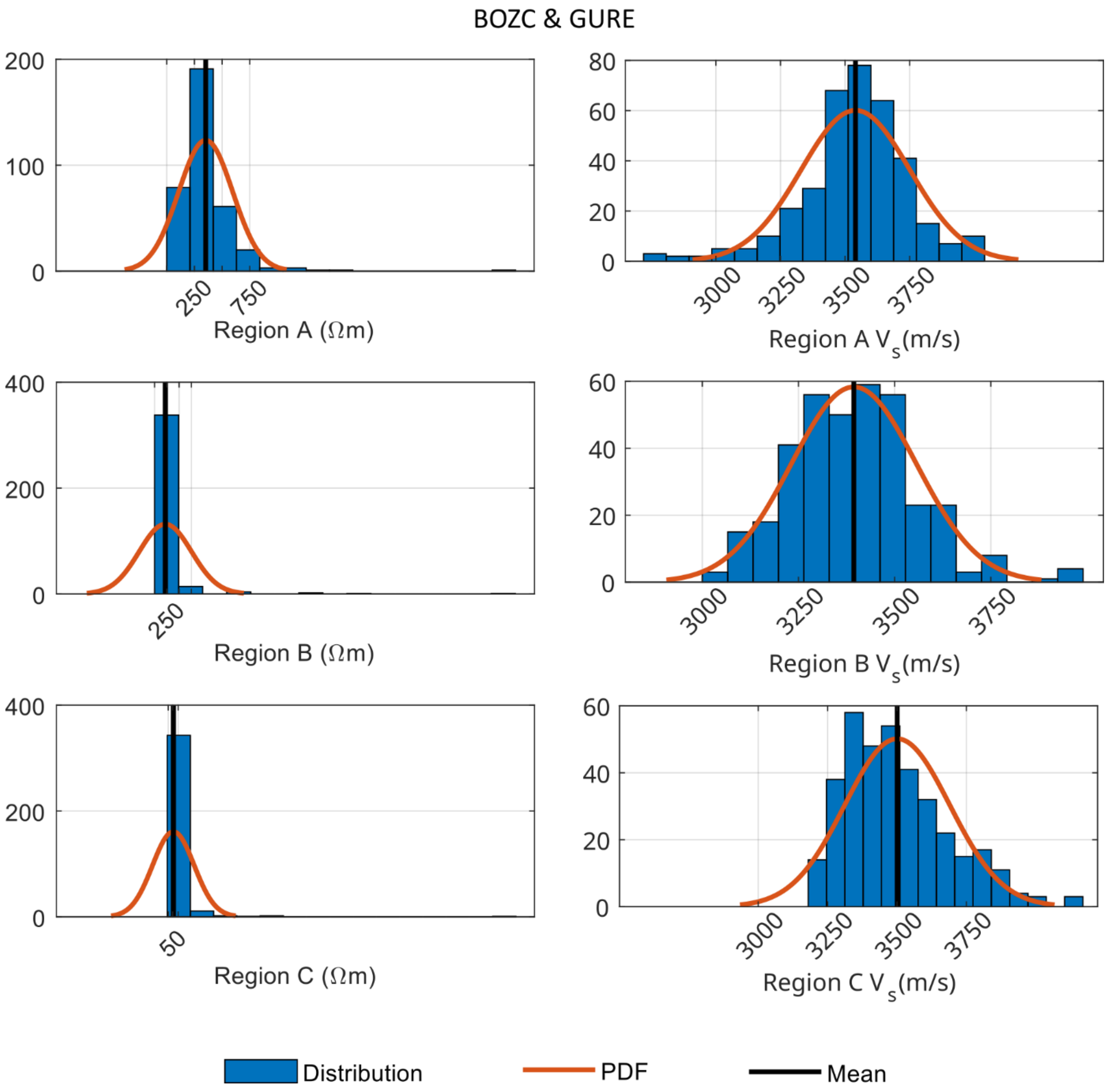

500 **Figure 13: Posteriori PDF of the resistivities (left), seismic velocities (right) and parameter obtained their *mP**-model in the region A, B and C for GB_p.**

Pareto optimality approach requires less computing time, however, PSO is very computationally intensive due to the large search area in the model space. The average computation time for 1000 iterations in each station was approximately three hours on a 14-core node of a central processing unit model, 12th generation Intel Core i7, 2.30 GHz with 64 GB RAM. The main difficulty in calculation time was calling the *gpdc.exe* function of the *SESARRAY* software package from *MATLAB*, which is the main programming platform that we used. One way to avoid the time-consuming calculations may be parallelize the code on a high-performance cluster (Pace et al., 2019a).

https://doi.org/10.5194/egusphere-2025-4698
Preprint. Discussion started: 26 September 2025

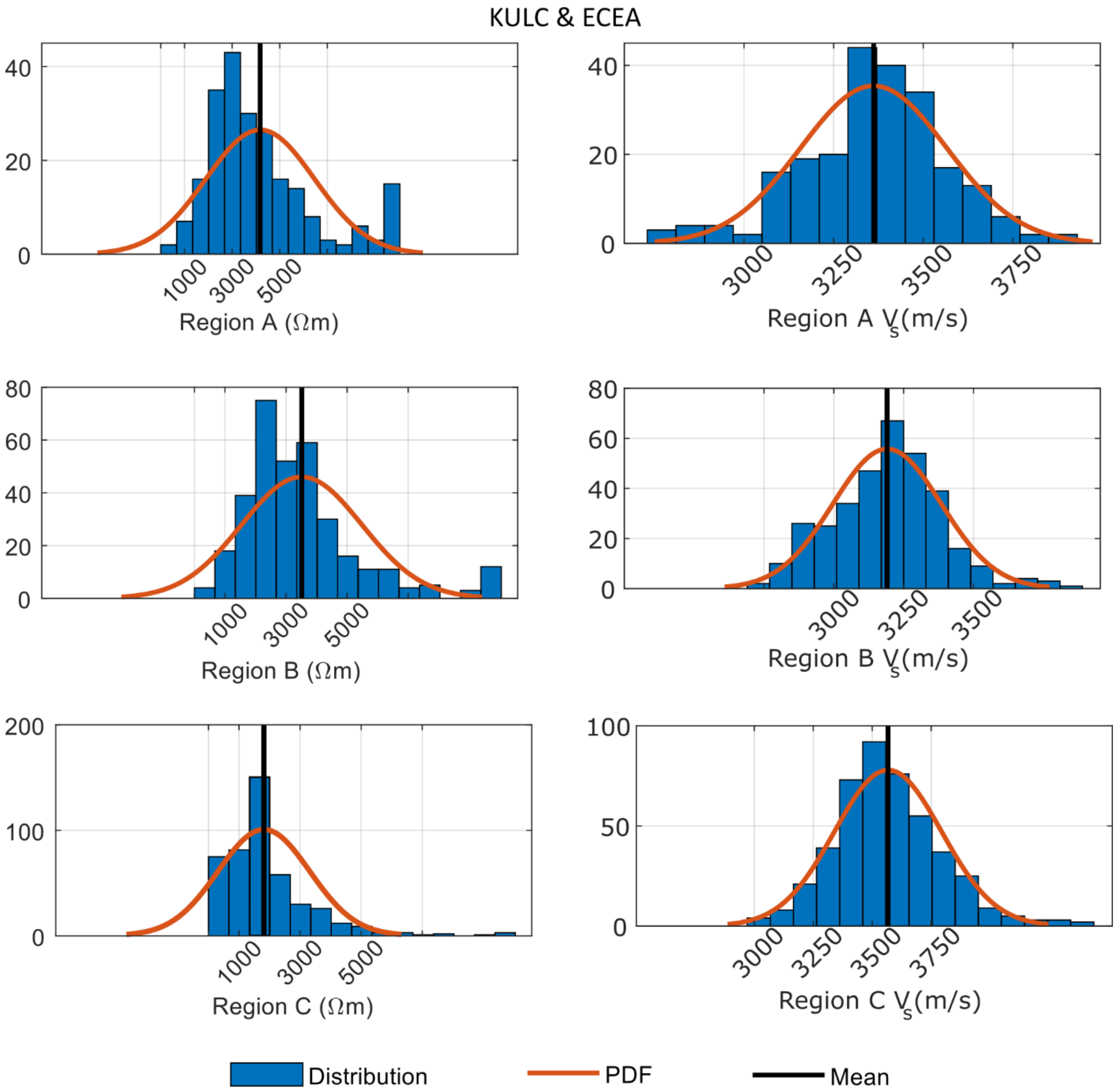

510 **Figure 14: Posteriori PDF of the resistivities (left), seismic velocities (right) and parameter obtained their *mP**-model in the region A, B and C for GB_p.**

515

Table 1: The sensitivity tests of regions A, B and C in the GB_p and KE_p solutions from updated Φ (%) by substituting with new model parameters.

GB_p	Subs (ohm.m)	Φ(%)	Subs (m/s)	Φ(%)	KE_p	Subs (ohm.m)	Φ(%)	Subs (m/s)	Φ(%)
A	750	3.2	3200	2.21	**A**	4000	1.2	3100	2.76
B	500	5.1	3500	3.39	**B**	5000	3.6	3500	3.26
C	100	3.15	3250	3.94	**C**	2000	2.16	3600	3.12

Acknowledgements

This work was supported by The Scientific and Technological Research Council of Türkiye (TÜBİTAK) under the 2218 National Postdoctoral Research Fellowship Programme, Project No. 118C550.

References

Afonso, J. C., Fullea, J., Griffin, W. L., Yang, Y., Jones, A. G., Connolly, J. A. D., and Reilly, S. Y. O.: 3-D multiobservable probabilistic inversion for the compositional andthermal structure of the lithosphere and upper mantle. I: A priori petrological information and geophysical observables, J Geophys Res Solid Earth, 118, 2586–2617, https://doi.org/10.1002/jgrb.50124, 2013.

Akca, I., Günther, T., Müller-Petke, M., Başokur, A. T., and Yaramanci, U.: Joint parameter estimation from magnetic resonance and vertical electric soundings using a multi-objective genetic algorithm, Geophys Prospect, 62, 364–376, https://doi.org/10.1111/1365-2478.12082, 2014.

Aldanmaz, E., Pearce, J. A., Thirlwall, M. F., and Mitchell, J. G.: Petrogenetic evolution of late Cenozoic, post-collision volcanism in western Anatolia, Turkey, Journal of Volcanology and Geothermal Research, 102, 67–95, https://doi.org/10.1016/S0377-0273(00)00182-7, 2000.

Altıner, D., Koçyiğit, A., Farinacci, A., Nicosia, U., and Conti, M. A.: Jurassic, Lower Cretaceous stratigraphy and paleogeographic evolution of the southern part of north-western Anatolia, Geologica Romana, 13–80, 1991.

Altunkaynak, Ş. and Genç, C.: Petrogenesis and time-progressive evolution of the Cenozoic continental volcanism in the Biga Peninsula, NW Anatolia (Turkey), Lithos, 102, 316–340, https://doi.org/10.1016/j.lithos.2007.06.003, 2008.

Altunkaynak, Ş., Dilek, Y., Genç, C. Ş., Sunal, G., Gertisser, R., Furnes, H., Foland, K. A., and Yang, J.: Spatial, temporal and geochemical evolution of Oligo-Miocene granitoid magmatism in western Anatolia, Turkey, https://doi.org/10.1016/j.gr.2011.10.010, 2012.

Amato, F., Pace, F., Vergnano, A., and Comina, C.: TDEM prospections for inland groundwater exploration in semiarid climate, Island of Fogo, Cape Verde, J Appl Geophy, 184, 104242, https://doi.org/10.1016/j.jappgeo.2020.104242, 2021.

https://doi.org/10.5194/egusphere-2025-4698
Preprint. Discussion started: 26 September 2025

Aquino, M., Marquis, G., and Vergne, J.: Joint one-dimensional inversion of magnetotelluric data and surface-wave dispersion curves using correspondence maps, Geophys Prospect, 70, 1455–1470, https://doi.org/10.1111/1365-2478.13239, 2022.

Aslan, Z., Erdem, D., Temizel, İ., and Arslan, M.: SHRIMP U–Pb zircon ages and whole-rock geochemistry for the Şapçı volcanic rocks, Biga Peninsula, Northwest Turkey: implications for pre-eruption crystallization conditions and source characteristics, Int Geol Rev, 59, 1764–1785, https://doi.org/10.1080/00206814.2017.1295282, 2017.

Bard, P.-Y.: Site EffectS assessments using AMbient Excitations (SESAME), European project reference EVG1-CT-2000-00026, 2000.

Baumgartner, U., Magele, C., and Renhart, W.: Pareto optimality and particle swarm optimization, IEEE Trans Magn, 40, 1172–1175, https://doi.org/10.1109/TMAG.2004.825430, 2004.

Beccaletto, L.: Geology, correlations, and geodynamic evolution of the Biga Peninsula (NW Turkey), PhD dissertation, University of Lausanne, Suisse, 2003.

Berdichevsky, M. N., Vanyan, L. L., and Dmitriev, V. I.: Methods used in the U.S.S.R. to reduce near-surface inhomogeneity effects on deep magnetotelluric sounding, Physics of the Earth and Planetary Interiors, 53, 194–206, https://doi.org/10.1016/0031-9201(89)90003-4, 1989.

Berteussen, K. A.: Moho depth determinations based on spectral-ratio analysis of NORSAR long-period P waves, Physics of the Earth and Planetary Interiors, 15, 13–27, https://doi.org/10.1016/0031-9201(77)90006-1, 1977.

Bijani, R., Lelièvre, P. G., Ponte-Neto, C. F., and Farquharson, C. G.: Physical-property-, lithology- And surface-geometry-based joint inversion using Pareto Multi-Objective Global Optimization, Geophys J Int, 209, 730–748, https://doi.org/10.1093/gji/ggx046, 2017.

Buttkus, B.: Spectral Analysis and Filter Theory in Applied Geophysics, 1st ed., Springer Berlin, Heidelberg, XV–667 pp., https://doi.org/10.1007/978-3-642-57016-2, 2000.

Büyük, E.: Pareto-Based Multiobjective Particle Swarm Optimization: Examples in Geophysical Modeling, in: Optimisation Algorithms and Swarm Intelligence, edited by: Vakhania, N. and Aydin, M. E., IntechOpen, Rijeka, Ch. 7, https://doi.org/10.5772/intechopen.97067, 2021.

Büyük, E.: A new method of smoothness-constrained magnetotelluric modelling with the utility of Pareto-optimal multi-objective particle swarm optimization, Geophys Prospect, 82, 1985–2004, https://doi.org/10.1111/1365-2478.13485, 2024.

Büyük, E. and Karaman, A.: Caprock integrity at Çanakkale-Tuzla hydrothermal system inferred from magnetotelluric modeling using particle swarm optimization, Geophysics, 89, 119–129, https://doi.org/10.1190/GEO2023-0192.1, 2024.

Buyuk, E., Zor, E., and Karaman, A.: Rayleigh wave dispersion curve inversion by using particle swarm optimization and genetic algorithm, 19th EGU General Assembly, EGU2017, proceedings from the conference held 23-28 April, 2017 in Vienna, Austria., p.6911, 19, 6911, 2017.

Büyük, E., Zor, E., and Karaman, A.: Joint modeling of rayleigh wave dispersion and H/V spectral ratio using pareto-based multiobjective particle swarm optimization, Turkish Journal of Earth Sciences, 29, 684–695, https://doi.org/10.3906/yer-2001-15, 2020.

Carcione, J. M., Ursin, B., and Nordskag, J. I.: Cross-property relations between electrical conductivity and the seismic velocity of rocks, Geophysics, 72, https://doi.org/10.1190/1.2762224, 2007.

Chave, A. D. and Jones, A. G.: The Magnetotelluric Method Theory and Practice, Cambridge University Press (CUP), New York, 1–584 pp., https://doi.org/http://dx.doi.org/10.1017/CBO9781139020138, 2012.

Chen, J., Hoversten, G. M., Key, K., Nordquist, G., and Cumming, W.: Stochastic inversion of magnetotelluric data using a sharp boundary parameterization and application to a geothermal site, Geophysics, 77, E265–E279, https://doi.org/10.1190/geo2011-0430.1, 2012.

Christensen, N. I. and Mooney, W. D.: Seismic velocity structure and composition of the continental crust: A global view, J Geophys Res Solid Earth, 100, 9761–9788, https://doi.org/10.1029/95JB00259, 1995.

Clerc, M. and Kennedy, J.: The particle swarm-explosion, stability, and convergence in a multidimensional complex space, IEEE Transactions on Evolutionary Computation, 6, 58–73, https://doi.org/10.1109/4235.985692, 2002.

Coello Coello, C. A., Pulido, G. T., and Lechuga, M. S.: Handling multiple objectives with particle swarm optimization, IEEE Transactions on Evolutionary Computation, 8, 256–279, https://doi.org/10.1109/TEVC.2004.826067, 2004.

Constable, S. C., Parker, R. L., and Constable, C. G.: Occam' s inversion: A practical algorithm for generating smooth models from electromagnetic sounding data, Geophysics, 52, 267–462, 1987.

Coxeter, H. S. M.: Regular polytopes, Dover Publications, 321 pp., 1973.

Dal Moro, G.: Insights on surface wave dispersion and HVSR: Joint analysis via Pareto optimality, J Appl Geophy, 72, 129–140, https://doi.org/10.1016/j.jappgeo.2010.08.004, 2010.

Dell'Aversana, P., Bernasconi, G., and Chiappa, F.: A Global Integration Platform for Optimizing Cooperative Modeling and Simultaneous Joint Inversion of Multi-domain Geophysical Data, AIMS Geosci, 2, 1–31, https://doi.org/10.3934/geosciences.2016.1.1, 2016.

Dewey, J. F. and Şengör, A. M. C.: Aegean and surrounding regions: Complex multiplate and continuum tectonics in a convergent zone, Bulletin of the Geological Society of America, 90, 84–92, https://doi.org/10.1130/0016-7606(1979)90<84:AASRCM>2.0.CO;2, 1979.

Dorman, J. and Ewing, M.: Numerical inversion of seismic surface wave dispersion data and crust-mantle structure in the New York-Pennsylvania area, J Geophys Res, 67, 5227–5241, https://doi.org/10.1029/JZ067I013P05227, 1962.

Eberhart, R. C. and Shi, Y.: Comparison between genetic algorithms and particle swarm optimization, in: Lecture Notes in Computer Science (including subseries Lecture Notes in Artificial Intelligence and Lecture Notes in Bioinformatics), 611–616, https://doi.org/10.1007/bfb0040812, 1998.

Eberhart-Phillips, D., Stanley, W. D., Rodriguez, B. D., and Lutter, W. J.: Surface seismic and electrical methods to detect fluids related to faulting, J Geophys Res Solid Earth, 100, 12919–12936, https://doi.org/10.1029/94JB03256, 1995.

Engelbrecht, A. P.: Computational Intelligence: An Introduction: Second Edition, John Wiley and Sons, 1–597 pp., https://doi.org/10.1002/9780470512517, 2007.

Essa, K. S. and Elhussein, M.: PSO (Particle Swarm Optimization) for Interpretation of Magnetic Anomalies Caused by Simple Geometrical Structures, Pure Appl Geophys, 175, 3539–3553, https://doi.org/10.1007/s00024-018-1867-0, 2018.

Essa, K. S., Mehanee, S. A., and Elhussein, M.: Gravity data interpretation by a two-sided fault-like geologic structure using the global particle swarm technique, Physics of the Earth and Planetary Interiors, 311, 106631, https://doi.org/10.1016/j.pepi.2020.106631, 2021.

Fan, H. and Shi, Y.: Study on Vmax of particle swarm optimization, in: Proceedings of the Workshop on Particle Swarm Optimization, 2001.

Fern, J. L. and Garc, E.: Appraising the Streaming-Potential Inverse Problem, Geophysics, 75, https://doi.org/10.1190/1.3460842, 2010.

Fernández Martínez, J. L., García Gonzalo, E., Fernández Álvarez, J. P., Kuzma, H. A., and Menéndez Pérez, C. O.: PSO: A powerful algorithm to solve geophysical inverse problems: Application to a 1D-DC resistivity case, J Appl Geophy, 71, 13–25, https://doi.org/10.1016/J.JAPPGEO.2010.02.001, 2010.

Fernández Martínez, J. L., Mukerji, T., García Gonzalo, E., and Suman, A.: Reservoir characterization and inversion uncertainty via a family of particle swarm optimizers, Geophysics, 77, 2334–2339, https://doi.org/10.1190/geo2011-0041.1, 2012.

Feucht, D. W., Sheehan, A. F., and Bedrosian, P. A.: Magnetotelluric Imaging of Lower Crustal Melt and Lithospheric Hydration in the Rocky Mountain Front Transition Zone, Colorado, USA, J Geophys Res Solid Earth, 122, 9489–9510, https://doi.org/10.1002/2017JB014474, 2017.

Friedrichs, B.: MAPROS, Time Series Manipulation, Metronix Measure- ment Instrument and Electronics Ltd., 1-126., 2007.

Fytikas, M., Giuliani, O., Innocenti, F., Marinelli, G., and Mazzuoli, R.: Geochronological data on recent magmatism of the Aegean Sea, Tectonophysics, 31, T29–T34, https://doi.org/10.1016/0040-1951(76)90161-X, 1976.

Gallardo, L. A.: Joint two-dimensional DC resistivity and seismic travel time inversion with cross-gradients constraints, J Geophys Res, 109, B03311, https://doi.org/10.1029/2003jb002716, 2004.

Gallardo, L. A. and Meju, M. A.: Characterization of heterogeneous near-surface materials by joint 2D inversion of dc resistivity and seismic data, Geophys Res Lett, 30, n/a-n/a, https://doi.org/10.1029/2003GL017370, 2003.

Gao, G., Abubakar, A., and Habashy, T. M.: Joint petrophysical inversion of electromagnetic and full-waveform seismic data, Geophysics, 77, https://doi.org/10.1190/geo2011-0157.1, 2012.

Garcia, K. and Diaz, D.: Three-dimensional geo-electrical structure in Juncalito geothermal prospect, northern Chile, Geothermics, 64, 527–537, https://doi.org/10.1016/j.geothermics.2016.08.001, 2016.

Garcia, X., Seillé, H., Elsenbeck, J., Evans, R. L., Jegen, M., Hölz, S., Ledo, J., Lovatini, A., Marti, A., Marcuello, A., Queralt, P., Ungarelli, C., and Ranero, C. R.: Structure of the mantle beneath the Alboran Basin from magnetotelluric soundings, Geochemistry, Geophysics, Geosystems, 16, 4261–4274, https://doi.org/10.1002/2015GC006100, 2015.

Gill, M. K., Kaheil, Y. H., Khalil, A., McKee, M., and Bastidas, L.: Multiobjective particle swarm optimization for parameter estimation in hydrology, Water Resour Res, 42, 1–14, https://doi.org/10.1029/2005WR004528, 2006.

Godio, A. and Santilano, A.: On the optimization of electromagnetic geophysical data: Application of the PSO algorithm, J Appl Geophy, 148, 163–174, https://doi.org/10.1016/j.jappgeo.2017.11.016, 2018.

Goldberg, D. E. and Holland, J. H.: Genetic Algorithms and Machine Learning, Mach Learn, 3, 95–99, https://doi.org/10.1023/A:1022602019183/METRICS, 1988.

Grandis, H. and Maulana, Y.: Particle Swarm Optimization (PSO) for Magnetotelluric (MT) 1D Inversion Modeling, IOP Conf Ser Earth Environ Sci, 62, https://doi.org/10.1088/1755-1315/62/1/012033, 2017.

Gupta, A. K., Mandal, P., Srinagesh, D., Tiwari, A., Sain, K., and Paul, A.: One-dimensional regional shear velocity structure from joint inversion of fundamental mode group velocity dispersion measurements of Love and Rayleigh waves: application to the Uttarakhand Himalaya, Acta Geophysica, 71, 2619–2632, https://doi.org/10.1007/S11600-023-01167-5/FIGURES/6, 2023a.

Gupta, R. K., Agrawal, M., and Pulliam, J.: Joint Modelling and Uncertainty Estimation for Site Characterization of Dhanbad City (India) Using Global Optimization, Pure Appl Geophys, 180, 3947–3969, https://doi.org/10.1007/S00024-023-03358-Z/FIGURES/11, 2023b.

Haber, E. and Oldenburg, D.: Joint inversion: A structural approach, Inverse Probl, 13, 63–77, https://doi.org/10.1088/0266-5611/13/1/006, 1997.

Hassan, R., Cohanim, B., De Weck, O., and Venter, G.: A comparison of particle swarm optimization and the genetic algorithm, in: Collection of Technical Papers - AIAA/ASME/ASCE/AHS/ASC Structures, Structural Dynamics and Materials Conference, 1138–1150, https://doi.org/10.2514/6.2005-1897, 2005.

Heise, W., Caldwell, T. G., Bibby, H. M., and Bannister, S. C.: Three-dimensional modelling of magnetotelluric data from the Rotokawa geothermal field, Taupo Volcanic Zone, New Zealand, Geophys J Int, 173, 740–750, https://doi.org/10.1111/j.1365-246X.2008.03737.x, 2008.

Hildreth, W. and Moorbath, S.: Crustal contributions to arc magmatism in the Andes of Central Chile, Contributions to Mineralogy and Petrology, 98, 455–489, https://doi.org/10.1007/BF00372365, 1988.

Hill, G. J., Caldwell, T. G., Heise, W., Chertkoff, D. G., Bibby, H. M., Burgess, M. K., Cull, J. P., and Cas, R. A. F.: Distribution of melt beneath Mount St Helens and Mount Adams inferred from magnetotelluric data, Nat Geosci, 2, 785–789, https://doi.org/10.1038/ngeo661, 2009.

Hu, B., Wen, L., and Zhou, X.: Joint inversion of VES and Rayleigh wave data based on improved DE algorithm for near surface exploration, World Journal of Engineering, 21, 242–253, https://doi.org/10.1108/WJE-05-2022-0193/FULL/PDF, 2024.

Karacık, Z. and Yılmaz, Y.: Geology of the Ignimbrites and the associated volcano-plutonic complex of The Ezine, Journal of Volcanology and Geothermal Research, 85, 251–264, 1998.

Karcıoğlu, G. and Gürer, A.: Implementation and model uniqueness of Particle Swarm Optimization method with a 2D smooth modeling approach for Radio-Magnetotelluric data, J Appl Geophy, 169, 37–48, https://doi.org/10.1016/j.jappgeo.2019.06.001, 2019.

Kennedy, J. and Eberhart, R.: Particle swarm optimization, Neural Networks, 1995. Proceedings., IEEE International Conference on, 4, 1942–1948 vol.4, https://doi.org/10.1109/ICNN.1995.488968, 1995.

Kennedy, J. and Spears, W. M.: Matching algorithms to problems: An experimental test of the particle swarm and some genetic algorithms on the multimodal problem generator, in: Proceedings of the IEEE Conference on Evolutionary Computation, ICEC, 78–83, https://doi.org/10.1109/icec.1998.699326, 1998.

Kirkpatrick, S., Gelatt, C. D., and Vecchi, M. P.: Optimization by Simulated Annealing, Science, New Series, 220, 671–680, 1983.

Kozlovskaya, E., Vecsey, L., Plomerova, J., and Raita, T.: Joint inversion of multiple data types with the use of multiobjective optimization: problem formulation and application to the seismic anisotropy investigations, Geophys J Int, 171, 761–779, https://doi.org/10.1111/j.1365-246X.2007.03540.x, 2007.

Kumar, V. and Minz, S.: Multi-Objective Particle Swarm Optimization: An Introduction, The Smart Computing Review, 4, 335–353, https://doi.org/10.6029/smartcr.2014.05.001, 2014.

Lee, S. J., Rhie, J., Kim, S., Kang, T. S., and Cho, C. S.: 1-D velocity model for the North Korean Peninsula from Rayleigh wave dispersion of ambient noise cross-correlations, J Seismol, 24, 121–131, https://doi.org/10.1007/S10950-019-09891-6/FIGURES/7, 2020.

Lelièvre, P. G., Farquharson, C. G., and Hurich, C. A.: Joint inversion of seismic traveltimes and gravity data on unstructured grids with application to mineral exploration, Geophysics, 77, 1JF-Z19, 2012.

Li, G., Cai, H., and Li, C. F.: Alternating Joint Inversion of Controlled-Source Electromagnetic and Seismic Data Using the Joint Total Variation Constraint, IEEE Transactions on Geoscience and Remote Sensing, 57, 5914–5922, https://doi.org/10.1109/TGRS.2019.2903043, 2019.

Linde, A. T. and Sacks, I. S.: Triggering of volcanic eruptions, Nature, 395, 888–890, 1998.

Lines, L. R., Schultz, A. K., and Treitel, S.: Cooperative inversion of geophysical data., Geophysics, 53, 8–20, https://doi.org/10.1190/1.1442403, 1988.

Liu, S., Liang, M., and Hu, X.: Particle swarm optimization inversion of magnetic data: Field examples from iron ore deposits in China, Geophysics, 83, J43–J59, https://doi.org/10.1190/geo2017-0456.1, 2018.

Manakou, M., Roumelioti, Z., and Riga, E.: Shear-wave velocity determination by combining data from passive and active source field investigations in Kumamoto city, Japan, Earth, Planets and Space, 75, 1–14, https://doi.org/10.1186/S40623-023-01916-2/FIGURES/8, 2023.

Manassero, M. C., Afonso, J. C., Zyserman, F., Zlotnik, S., and Fomin, I.: A reduced order approach for probabilistic inversions of 3-D magnetotelluric data I: general formulation, Geophys J Int, 223, 1837–1863, https://doi.org/10.1093/gji/ggaa415, 2020.

Mavko, G., Mukerji, T., and Dvorkin, J.: The Rock Physics Handbook: Tools for Seismic Analysis in Porous Media, Cambridge University Press, 208–210 pp., 1998.

McKenzie, D.: Active tectonics of the Alpine—Himalayan belt: the Aegean Sea and surrounding regions, Geophysical Journal of the Royal Astronomical Society, 55, 217–254, https://doi.org/10.1111/j.1365-246X.1978.tb04759.x, 1978.

McKenzie, D. and Yılmaz, Y.: Deformation and volcanism in Western Turkey and the Aegean, Bull. Tech. Univ. Istanbul, 44, 345–373, 1991.

McMechan, G. A. and Yedlin, M. J.: Analysis of dispersive by wave field transformation, Geophysics, 46, 869–874, https://doi.org/10.1190/1.1441225, 1981.

Meju, M. A. and Gallardo, L. A.: Structural Coupling Approaches in Integrated Geophysical Imaging, Integrated Imaging of the Earth: Theory and Applications, 49–67, https://doi.org/10.1002/9781118929063.ch4, 2016.

Monteiro Santos, F. A.: Inversion of self-potential of idealized bodies' anomalies using particle swarm optimization, Comput Geosci, 36, 1185–1190, https://doi.org/10.1016/j.cageo.2010.01.011, 2010.

Moore, H. L.: Cours d'Économie Politique. By VILFREDO PARETO, Professeur à l'Université de Lausanne. Vol. I. Pp. 430. I896. Vol. II. Pp. 426. I897. Lausanne: F. Rouge, Ann Am Acad Pol Soc Sci, 9, 128–131, https://doi.org/10.1177/000271629700900314, 1897.

Moorkamp, M., Jones, A. G., and Eaton, D. W.: Joint inversion of teleseismic receiver functions and magnetotelluric data using a genetic algorithm: Are seismic velocities and electrical conductivities compatible?, Geophys Res Lett, 34, 3–7, https://doi.org/10.1029/2007GL030519, 2007.

Moorkamp, M., Jones, A. G., and Fishwick, S.: Joint inversion of receiver functions, surface wave dispersion, and magnetotelluric data, J Geophys Res Solid Earth, 115, 1–23, https://doi.org/10.1029/2009JB006369, 2010.

Moorkamp, M., Roberts, A. W., Jegen, M., Heincke, B., and Hobbs, R. W.: Verification of velocity-resistivity relationships derived from structural joint inversion with borehole data, Geophys Res Lett, 40, 3596–3601, https://doi.org/10.1002/grl.50696, 2013.

Naidu, G. D.: Magnetotellurics: Basic Theoretical Concepts, in: Deep Crustal Structure of the Son-Narmada-Tapti Lineament, Central India, edited by: Naidu, G. D., Springer Berlin Heidelberg, Berlin, Heidelberg, 13–35, https://doi.org/10.1007/978-3-642-28442-7_2, 2012.

Nakajima, J., Matsuzawa, T., Hasegawa, A., and Zhao, D.: Seismic imaging of arc magma and fluids under the central part of northeastern Japan, Tectonophysics, 341, 1–17, https://doi.org/10.1016/S0040-1951(01)00181-0, 2001.

Ogaya, X., Alcalde, J., Marzán, I., Ledo, J., Queralt, P., Marcuello, A., Martí, D., Saura, E., Carbonell, R., and Benjumea, B.: Joint interpretation of magnetotelluric, seismic, and well-log data in Hontomín (Spain), Solid Earth, 7, 943–958, https://doi.org/10.5194/SE-7-943-2016, 2016.

Okada, T., Matsuzawa, T., Nakajima, J., Uchida, N., Yamamoto, M., Hori, S., Kono, T., Nakayama, T., Hirahara, S., and Hasegawa, A.: Seismic velocity structure in and around the Naruko volcano, NE Japan, and its implications for volcanic and seismic activities Geofluid processes in subduction zones and mantle dynamics 4. Seismology, Earth, Planets and Space, 66, 1–10, https://doi.org/10.1186/1880-5981-66-114/FIGURES/8, 2014.

Okay, A. I. and Satir, M.: Upper Cretaceous eclogite-facies metamorphic rocks from the Biga Peninsula, Northwest Turkey, Turkish Journal of Earth Sciences, 9, 47–56, 2000.

Okay, A. I., Satir, M., Maluski, H., Siyako, M., Monie, P., Metzger, R., and Akyüz, S.: Paleo- and Neo-Tethyan events in northwest Turkey: geological and geochronological constraints, in: The Tectonic Evolution of Asia, edited by: Yin, A. and Harrison, T. M., Cambridge University Press, 420–441, 1996.

Özalaybey, S., Zor, E., Ergintav, S., and Tapirdamaz, M. C.: Investigation of 3-D basin structures in the İzmit Bay area (Turkey) by single-station microtremor and gravimetric methods, Geophys J Int, 186, 883–894, https://doi.org/10.1111/j.1365-246X.2011.05085.x, 2011.

Paasche, H. and Tronicke, J.: Cooperative inversion of 2D geophysical data sets: A zonal approach based on fuzzy c-means cluster analysis, Geophysics, 72, https://doi.org/10.1190/1.2670341, 2007.

Pace, F., Godio, A., Santilano, A., and Comina, C.: Joint optimization of geophysical data using multi-objective swarm intelligence, Geophys J Int, 218, 1502–1521, https://doi.org/10.1093/gji/ggz243, 2019a.

Pace, F., Santilano, A., and Godio, A.: Particle swarm optimization of 2D magnetotelluric data, Geophysics, 84, E125–E141, https://doi.org/10.1190/geo2018-0166.1, 2019b.

Pace, F., Santilano, A., and Godio, A.: A Review of Geophysical Modeling Based on Particle Swarm Optimization, https://doi.org/10.1007/s10712-021-09638-4, 1 May 2021.

Pace, F., Raftogianni, A., and Godio, A.: A Comparative Analysis of Three Computational-Intelligence Metaheuristic Methods for the Optimization of TDEM Data, Pure Appl Geophys, 179, 3727–3749, https://doi.org/10.1007/s00024-022-03166-x, 2022.

Pallero, J. L. G., Fernanndez-Martinez, J. L., Bonvalot, S., and Fudym, O.: Gravity inversion and uncertainty assessment of basement relief via Particle Swarm Optimization, J Appl Geophy, 116, 180–191, https://doi.org/10.1016/j.jappgeo.2015.03.008, 2015.

Peksen, E., Yas, T., Kayman, A. Y., and Özkan, C.: Application of particle swarm optimization on self-potential data, J Appl Geophy, 75, 305–318, https://doi.org/10.1016/j.jappgeo.2011.07.013, 2011.

Peksen, E., Yas, T., and Kiyak, A.: 1-D DC Resistivity Modeling and Interpretation in Anisotropic Media Using Particle Swarm Optimization, Pure Appl Geophys, 171, 2371–2389, https://doi.org/10.1007/s00024-014-0802-2, 2014.

Rao, S. S.: Engineering Optimization: Theory and Practice: Fourth Edition, John Wiley & Sons, Inc., Hoboken, NJ, USA, 1–813 pp., https://doi.org/10.1002/9780470549124, 2009.

Reyes-Sierra, M. and Coello Coello, C. a.: Multi-Objective Particle Swarm Optimizers: A Survey of the State-of-the-Art, International Journal of Computational Intelligence Research, 2, 287–308, https://doi.org/10.5019/j.ijcir.2006.68, 2006.

Romano, G., Balasco, M., Siniscalchi, A., Gueguen, E., Petrillo, Z., and Tripaldi, S.: Geological and geo-structural characterization of the Montemurro area (Southern Italy) inferred from audiomagnetotelluric survey, Geomatics, Natural Hazards and Risk, 9, 1156–1171, https://doi.org/10.1080/19475705.2018.1502210, 2018.

Roux, E., Moorkamp, M., Jones, A. G., Bischoff, M., Endrun, B., Lebedev, S., and Meier, T.: Joint inversion of long-period magnetotelluric data and surface-wave dispersion curves for anisotropic structure: Application to data from Central Germany, Geophys Res Lett, 38, https://doi.org/10.1029/2010GL046358, 2011a.

Roux, E., Moorkamp, M., Jones, A. G., Bischoff, M., Endrun, B., Lebedev, S., and Meier, T.: Joint inversion of long-period magnetotelluric data and surface-wave dispersion curves for anisotropic structure: Application to data from Central Germany, Geophys Res Lett, 38, 1–5, https://doi.org/10.1029/2010GL046358, 2011b.

S. Zhdanov, M.: Magnetotelluric and Magnetovariational Methods, Foundations of Geophysical Electromagnetic Theory and Methods, 495–584, https://doi.org/10.1016/B978-0-44-463890-8.00017-7, 2018.

Sambridge, M.: Geophysical inversion with a neighbourhood algorithm—II. Appraising the ensemble, Geophys J Int, 138, 727–746, https://doi.org/10.1046/J.1365-246X.1999.00900.X, 1999.

Scherbaum, F., Hinzen, K. G., and Ohrnberger, M.: Determination of shallow shear wave velocity profiles in the cologne, Germany area using ambient vibrations, Geophys J Int, 152, 597–612, https://doi.org/10.1046/j.1365-246X.2003.01856.x, 2003.

Schnaidt, S., Conway, D., Krieger, L., and Heinson, G.: Pareto-Optimal Multi-objective Inversion of Geophysical Data, Pure Appl Geophys, 175, 2221–2236, https://doi.org/10.1007/s00024-018-1784-2, 2018.

Şengün, F., Yiğitbaş, E., and Tunç, I. O.: Geology and tectonic emplacement of eclogite and Blueschists, Biga Peninsula, northwest turkey, Turkish Journal of Earth Sciences, 20, 273–285, https://doi.org/10.3906/yer-0912-75, 2011.

Seyitoğlu, G. and Scott, B. C.: Late Cenozoic crustal extension and basin formation in west Turkey, Geol Mag, 128, 155–166, https://doi.org/10.1017/S0016756800018343, 1991.

Shaw, R. and Srivastava, S.: Particle swarm optimization: A new tool to invert geophysical data, Geophysics, 72, F75, https://doi.org/10.1190/1.2432481, 2007.

Simpson, F. and Bahr, K.: Practical Magnetotellurics, Press Syndicate of the University of Cambridge, 2005.

Siripunvaraporn, W., Egbert, G., Lenbury, Y., and Uyeshima, M.: Three-dimensional magnetotelluric inversion: Data-space method, Physics of the Earth and Planetary Interiors, 150, 3–14, https://doi.org/10.1016/j.pepi.2004.08.023, 2005.

Smirnov, M. Y.: Magnetotelluric data processing with a robust statistical procedure having a high breakdown point, Geophys J Int, 152, 1–7, https://doi.org/10.1046/j.1365-246X.2003.01733.x, 2003.

Smith, J. T. and Booker, J. R.: Magnetotelluric inversion for minimum structure, Geophysics, 53, 1565–1576, https://doi.org/10.1190/1.1442438, 1988.

Song, X., Tang, L., Lv, X., Fang, H., and Gu, H.: Application of particle swarm optimization to interpret Rayleigh wave dispersion curves, J Appl Geophy, 84, 1–13, https://doi.org/10.1016/j.jappgeo.2012.05.011, 2012.

Stanley, W. D., Boehl, J. E., Bostick, F. X., and Smith, H. W.: Geothermal significance of magnetotelluric sounding in the Eastern Snake River Plain-Yellowstone Region, J Geophys Res, 82, 2501–2514, https://doi.org/10.1029/JB082i017p02501, 1977.

Stefano, M. De, Andreasi, F. G., Re, S., Virgilio, M., and Snyder, F. F.: Multiple-domain, simultaneous joint inversion of geophysical data with application to subsalt imaging, Geophysics, 76, https://doi.org/10.1190/1.3554652, 2011.

Takei, Y.: Constitutive mechanical relations of solid-liquid composites in terms of grain-boundary contiguity, J Geophys Res Solid Earth, 103, 18183–18203, https://doi.org/10.1029/98JB01489, 1998.

Takougang, E. M. T., Harris, B., Kepic, A., and Le, C. V. A.: Cooperative joint inversion of 3D seismic and magnetotelluric data: With application in a mineral province, Geophysics, 80, R175–R187, https://doi.org/10.1190/geo2014-0252.1, 2015.

Taymaz, T., Jackson, J., and McKenzie, D.: Active tectonics of the north and central Aegean Sea, Geophys J Int, 106, 433–490, https://doi.org/10.1111/j.1365-246X.1991.tb03906.x, 1991.

Tietze, K. and Ritter, O.: Three-dimensional magnetotelluric inversion in practice—the electrical conductivity structure of the San Andreas Fault in Central California, Geophys J Int, 195, 130–147, https://doi.org/10.1093/GJI/GGT234, 2013.

Tronicke, J., Paasche, H., and Boniger, U.: Join global inversion of GPR and P-wave seismic traveltimes using particle swarm optimization, 2011 6th International Workshop on Advanced Ground Penetrating Radar, IWAGPR 2011, https://doi.org/10.1109/IWAGPR.2011.5963884, 2011.

Turunçtur, B., Eken, T., Chen, Y., Taymaz, T., Houseman, G. A., and Saygin, E.: Crustal velocity images of northwestern Türkiye along the North Anatolian Fault Zone from transdimensional Bayesian ambient seismic noise tomography, Geophys J Int, 234, 636–649, https://doi.org/10.1093/gji/ggad082, 2023.

Vozoff, K.: Magnetotellurics: Principles and practice, Proceedings of the Indian Academy of Sciences - Earth and Planetary Sciences, 99, 441–471, https://doi.org/10.1007/BF02840313/METRICS, 1990.

Wagner, F. M. and Uhlemann, S.: An overview of multimethod imaging approaches in environmental geophysics, Advances in Geophysics, 62, 1–72, https://doi.org/10.1016/bs.agph.2021.06.001, 2021.

Wu, P., Tan, H., Peng, M., Ma, H., and Wang, M.: Joint Inversion of 1-D Magnetotelluric and Surface-Wave Dispersion Data with an Improved Multi-Objective Genetic Algorithm and Application to the Data of the Longmenshan Fault Zone, Pure Appl Geophys, 175, 3591–3604, https://doi.org/10.1007/s00024-018-1884-z, 2018.

Wu, P., Tan, H., Lin, C., Peng, M., Ma, H., and Yan, Z.: Joint inversion of two-dimensional magnetotelluric and surface wave dispersion data with cross-gradient constraints, Geophys J Int, 221, 938–950, https://doi.org/10.1093/GJI/GGAA045, 2020.

Wu, P., Tan, H., Ding, Z., Kong, W., Peng, M., Wang, X., and Xu, L.: Joint inversion of 3-D magnetotelluric and ambient noise dispersion data sets with cross-gradient constraints: methodology and application, Geophys J Int, 230, 714–732, https://doi.org/10.1093/gji/ggac049, 2022.

Yang, X., Keppler, H., McCammon, C., and Ni, H.: Electrical conductivity of orthopyroxene and plagioclase in the lower crust, Contributions to Mineralogy and Petrology, 163, 33–48, https://doi.org/10.1007/S00410-011-0657-9/FIGURES/10, 2012.

Yilmaz, Y.: Comparison of young volcanic associations of western and eastern Anatolia formed under a compressional regime: a review, Journal of Volcanology and Geothermal Research, 44, 69–87, https://doi.org/10.1016/0377-0273(90)90012-5, 1990.

Yilmaz, Y., Genç, Ş. C., Karacik, Z., and Altunkaynak, Ş.: Two contrasting magmatic associations of NW Anatolia and their tectonic significance, J Geodyn, 31, 243–271, https://doi.org/10.1016/S0264-3707(01)00002-3, 2001.

Yuan, S., Wang, S., and Tian, N.: Swarm intelligence optimization and its application in geophysical data inversion, Applied Geophysics, 6, 166–174, https://doi.org/10.1007/s11770-009-0018-x, 2009.

Zhao, D., Mishra, O. P., and Sanda, R.: Influence of fluids and magma on earthquakes: seismological evidence, Physics of the Earth and Planetary Interiors, 132, 249–267, https://doi.org/10.1016/S0031-9201(02)00082-1, 2002.